ANNUAL REPORT[1]

Fundamentals of Energy Transport in Nanofluids
DE-FG02-04ER46101

[November 1, 2003 – July 31, 2004]

Submitted by

PI: Kenneth D. Kihm[2], Professor
Department of Mechanical Engineering
Texas A&M University
College Station, TX 77843-3123

To

Dr. Timothy J. Fitzsimmons
Department of Energy
Division of Materials Sciences and Engineering
Office of Basic Energy Sciences
Washington, DC 20585

July 31, 2004

[1] This report is also considered as Final Report since the grant is de-obligated from Texas A&M University due to the PI's transfer to the University of Tennessee. Continuation of the project will be submitted as a new proposal requesting re-obligation at the University of Tennessee.

[2] Presently at University of Tennessee, Mechanical, Aerospace and Biomedical Engineering Department, Knoxville, TN 37996-2210: Tel. (865) 974-5292, E-mail: kkihm@utk.edu

A. PROGRESS REPORT
[November 1, 2003 ~ July 31, 2004]

1. Associated Personnel

Researcher and PI:	Prof. K. D. Kihm, Texas A&M University
Visiting Researcher (01/04 – 07/04):	Prof. S. P. Lee, Kyonggi University, Korea
Visiting Researcher (09/03 – 02/04):	Prof. T. Takagi, Kushiro University, Japan
Graduate Research Assistant:	Mr. C. H. Chon, Texas A&M University

2. Research Objectives

Development and applications of nanoparticle analyzing techniques to examine their thermal behaviors in suspension, including the thermal conductivity, thermal (Brownian) diffusion, thermophoresis and thermocapillaryphoresis.

3. Itemized Progress

3-1. Development of a new miniaturized heated-wire conductivity measurement system

Thermal conductivity measurements for CuO and Al_2O_3 nanofluids have been performed with a newly-developed miniaturized heated-wire conductivity measurement device that require 10-ml capacity versus the first generation Argonne National Laboratory's system requiring 50-ml sample. The current data confirmed, within acceptable discrepancies, previously published data obtained by other research groups (Lee et al.[3] 1999, Das et al.[4] 2003) under identical conditions. Thus, the measurement accuracy of the newly developed miniaturized device has been validated. More detailed report is presented in **Appendix 1**.

3-2. Identification of surfactant effect on thermal conductivity

When nanoparticles are mixed with base fluid, adding surfactant is essential to enhance the dispersion and minimize the coagulation of nanoparticles. Additionof surfactant, however, can unfavorably change the thermal characteristics of nanofluids. Using the developed miniaturized system, measurements have been made for thermal conductivities of nanofluids with surfactants. The results persistently show substantial decreases of the thermal conductivity in comparison with nanofluids with no surfactant mixed. In order to find the physical explanation for the reduced conductivity, both experimental and analytical studies are carefully explored to be implemented. More detailed report is presented in **Appendix 2**.

[3] Lee, S, Choi, S.U.S., Li, S., and Eastman, J.A., 1999, "Measuring Thermal Conductivity of Fluids Containing Oxide Nano-Particles," Journal of Heat Transfer, Vol. 121, pp. 280-289.

[4]

3-3. Development of optical tracking of nanoparticle phoreses in suspension

Nanoparticle tracking optical system has been developed using the concept based on Microscopic Particle Image Velocimetry (μ-PIV). Brownian motions of suspended nanoparticles have been successfully recorded by a microscopic imaging CCD and the images are being analyzed to compare the Brownian motion in fluid with and without surfactants. Dr. Kihm's laboratory has already developed a particle tracking algorithm which can analyze the recorded images for the dynamic behavior of nanoparticles. More detailed report is presented in **Appendix 3**.

4. Publications/Presentations/Awards

Refereed Journal Publications:

K. D. Kihm, A. Banerjee, C. K. Choi, and T. Takagi, "Near-Wall Hindered Brownian Diffusion of Nanoparticles Examined By Three-Dimensional Ratiometric Total Internal Reflection Fluorescence Microscopy (3D R-TIRFM)," *Experiments in Fluids* (accepted for publication) – the accepted manuscript is presented in **Appendix 4**.

Conference Proceeding Publications:

K. D. Kihm and A. Banerjee, "Tracking of Nanoparticles Using Evanescenet Wave Microscopy," HT-FED2004-56652, 2004 ASME-HTFE Summer Conference, Charlotte, North Carolina, July 2004.

K. D. Kihm, J.-S. Park and C.-K. Choi, "Nano-PTV Using Confocal Microscopy," HT-FED2004-56653, 2004 ASME-HTFE Summer Conference, Charlotte, North Carolina, July 2004.

Presentations:

"Can we track nanoparticles in micro/nano-scale resolution?," K. D. Kihm, 2003 Korean Society of Visualization Conference, Pohang, Korea, November 14, 2003.

"Three-dimensional tracking of nanoparticles for micro/nano/bio-fluidic applications," K. D. Kihm, International Symposium on Particle Image Velocimetry Web Laboratory 2004, Kanazawa, Japan, January 14, 2004.

"Full-Field Optical Tracking of Nanoparticles In Micro/Nano-Scale Resolution," K. D. Kihm, BioMedical Engineering, Texas A&M University, January 26, 2004.

"Three-Dimensional Tracking of Nanoparticles for Micro/Nano/Bio-Fluidic Applications," K. D. Kihm, University of Tennessee, February 12, 2004.

"Why and how do we track thermal behaviors of nanoparticles in micro/nano-scale resolution?" K. D. Kihm, National Science Foundation-CTS Division, Arlington, VA, May 27, 2004.

B. SUMMARY OF FUTURE RESEARCH
[August 1, 2004 ~ October 31, 2006]

1. Rationale for Future Research

The rationale for future research is two-fold in that the primary focus will be to discover the fundamental energy transport mechanisms for nanoparticle suspension. Using the diagnostic techniques developed during the first year, carefully planned experimental investigations will be conducted to delineate both fundamental reasons for the reduced conductivity by surfactant and to establish quantitative characteristics for the nanoparticle phoreses under temperature gradients.

1-1. Fundamental reasons for nanofluidic conductivity degradation by surfactant:

It has been previously conjectured that the "coated" surfactant on the nanoparticle surface can be considered as an insulator to act to degrade the thermal conductivity. The conjecture, however, remains lacking formidable physical evidence. In order to analytically examine the conjecture, the existing theory will be extended to predict the effect of the surfactant layer on the effective conductivity using available thermal and mechanical properties of surfactant, nanoparticles and surrogating fluid. The surfactant coated nanoparticles will also reduce their Brownian motion because of their relatively enlarged sizes. The Brownian motion of identical nanoparticles suspended in two different fluids, nanofluids with and then without surfactant, will be measured using the imaging and processing technique described in Section 3-3 in Chapter A. The results will confirm the conjecture of the conductivity degradation due to the enlarged sizes and will also lead to quantitative explanation for the correlation between the surfactant effect and the thermal conductivities of nanofluids. Experiments will be repeated for different nanoparticles (Al_2O_3, CuO, SWNT etc.) at different volume concentrations.

1-2. Fundamental mechanism of nanofluidic energy transport – thermal, thermophoretic and thermocapillary phoretic behaviors

The thermophoresis of nanoparticles under a specified temperature gradient will be measured and analyzed for setting up a correlation between the particle motions and thermal conductivities of nanofluids. Measurements will include the Brownina thermal motion at different suspension temperatures, thermophoresis motion for differently specified temperature gradients inside suspension liquid, and thermocapillary phoresis of nanoparticles along the gas-nanofluid interface with temperature differential is provided along the interfacial meniscus inside a capillary pore. The expected results will lead to describe the fundamental mechanism for nanofluidic energy transport by thermal conduction, bulk convection and interfacial convection, respectively.

2. Associated Personnel

Researcher and PI:	Prof. K. D. Kihm[5], University of Tennessee
Graduate Research Assistant:	Mr. C. H. Chon, University of Tennessee

3. List of Federal Support

Current:

1. US DOE-Basic Energy Science Program/Argonne National Laboratory (2003-2006); Fundamentals of Energy Transport in Nanofluids-Phase II; K. D. Kihm (Co-PI), $173,523. (Present Award)

2. NASA Fluid Physics: Research and Flight Experiment Opportunity (2001-2005); Microscale Investigation of the Thermo-Fluid Transport in the Transition Film Region of an Evaporating Capillary Meniscus Using a Microgravity Environment; K. D. Kihm (PI), $348,857.

3. AFOSR/WP-AFB (2002-2005); Microscale Investigation of High-Temperature Heat Pipes and Capillary Pumping Loops; K. D. Kihm (PI), $200,000.

Pending:

None

[5] PI, together with GRA, will transfer to University of Tennessee as of August 1, 2004.

Appendix 1. A New Miniaturized Heated-Wire Conductivity Measurement System

Figure A-1 shows the experimental setup for thermal conductivity measurements including a miniaturized heated-wire device (1), a signal amplifier (2), and a precision dc power supplier (3).

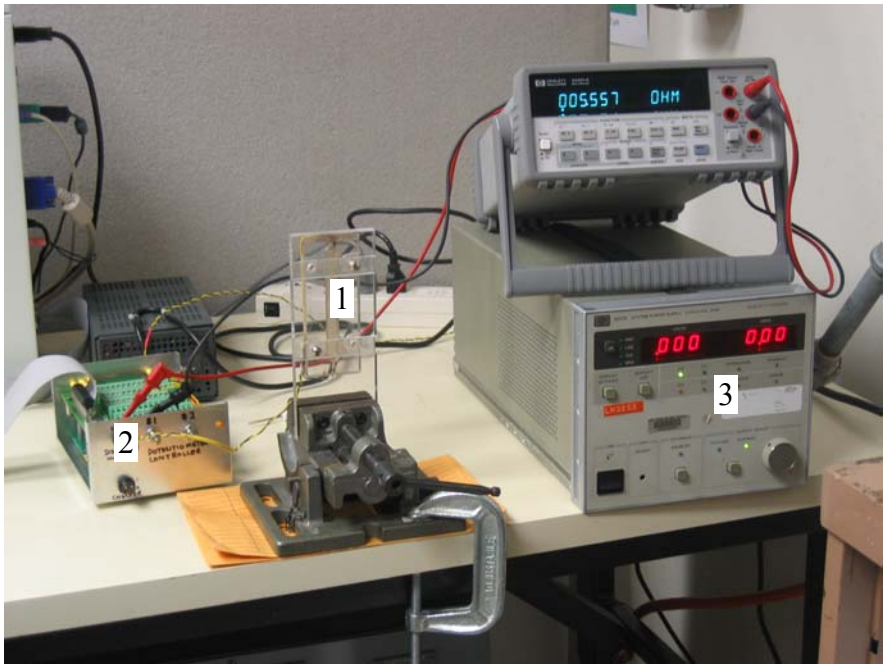

(a) Overview of the experimental setup

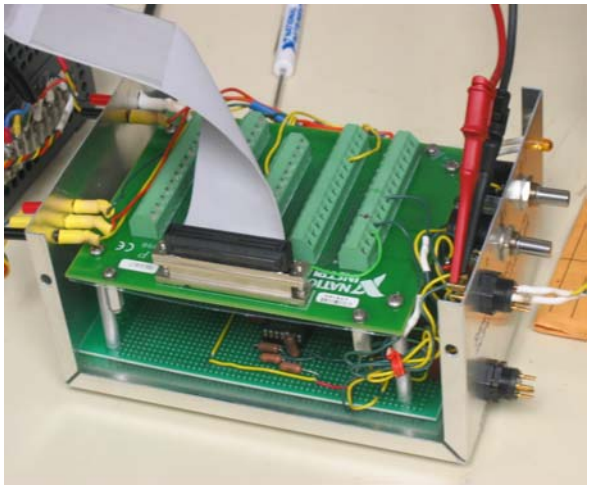

(b) Signal amplifier

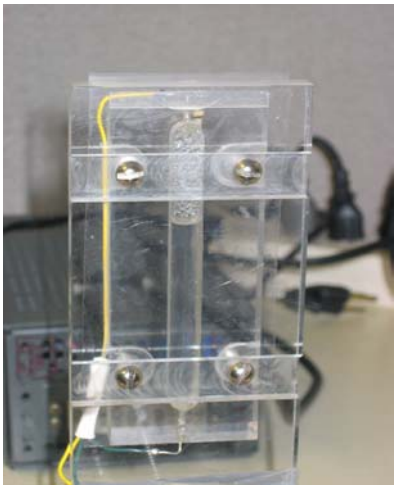

(c) Miniaturized heated-wire device

Figure A-1. Experimental setup for thermal conductivity measurements

The measurement accuracy was verified by using distilled water as a test fluid (listed conductivity of 0.628W/mK at 37ºC) and obtaining the measured thermal conductivity of 0.6286W/mK ± 0.0098 W/mK. Table A-1 summarizes the measurement uncertainties.

Table A-1. Sources of uncertainty

	Measured value	Uncertainty	
		System, B_x	Measurement, P_x
Supplied heat (W), q	0.9798	2.09×10^{-3}	4.327×10^{-6}
Wire length (m), l	0.095	0.001	0.001
Data Slope, s	1.0701	0.02527	1.9×10^{-5}

The nanofluids for the experiment must be ensured for proper dispersion of nanoparticles and a proper pH value to attain the dispersion and stability of the suspension against sedimentation. The nanofluids supplied by Nanophase Technology Corporation consists of unknown dispersant (The company is reluctant to reveal information on the type and concentration of the dispersant). The average particle sizes are 29-nm for CuO and 47-nm for Al_2O_3 (Fig. A-2).

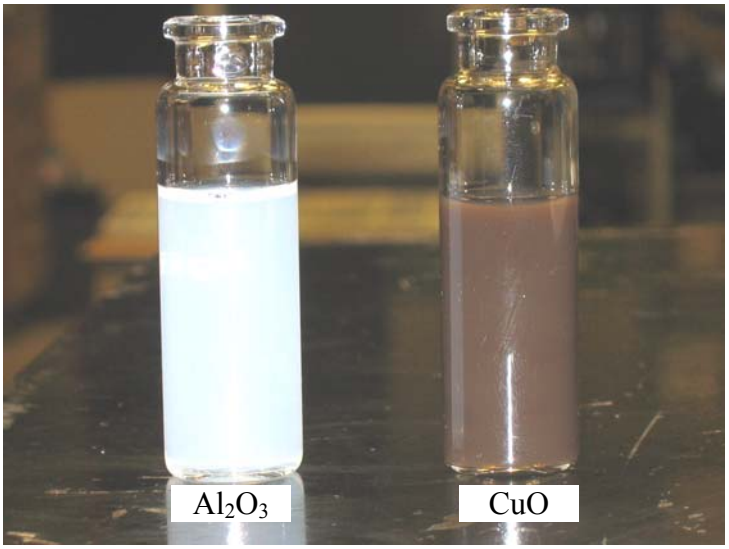

Figure A-2. Sample nanofluids containing Al_2O_3 and CuO

Figure A-3 shows good agreement of the measured thermal conductivity with previously published data by Argonne National Laboratory (Lee et al. 1999), for the range of volume concentration from 0 to 5% at room temperature.

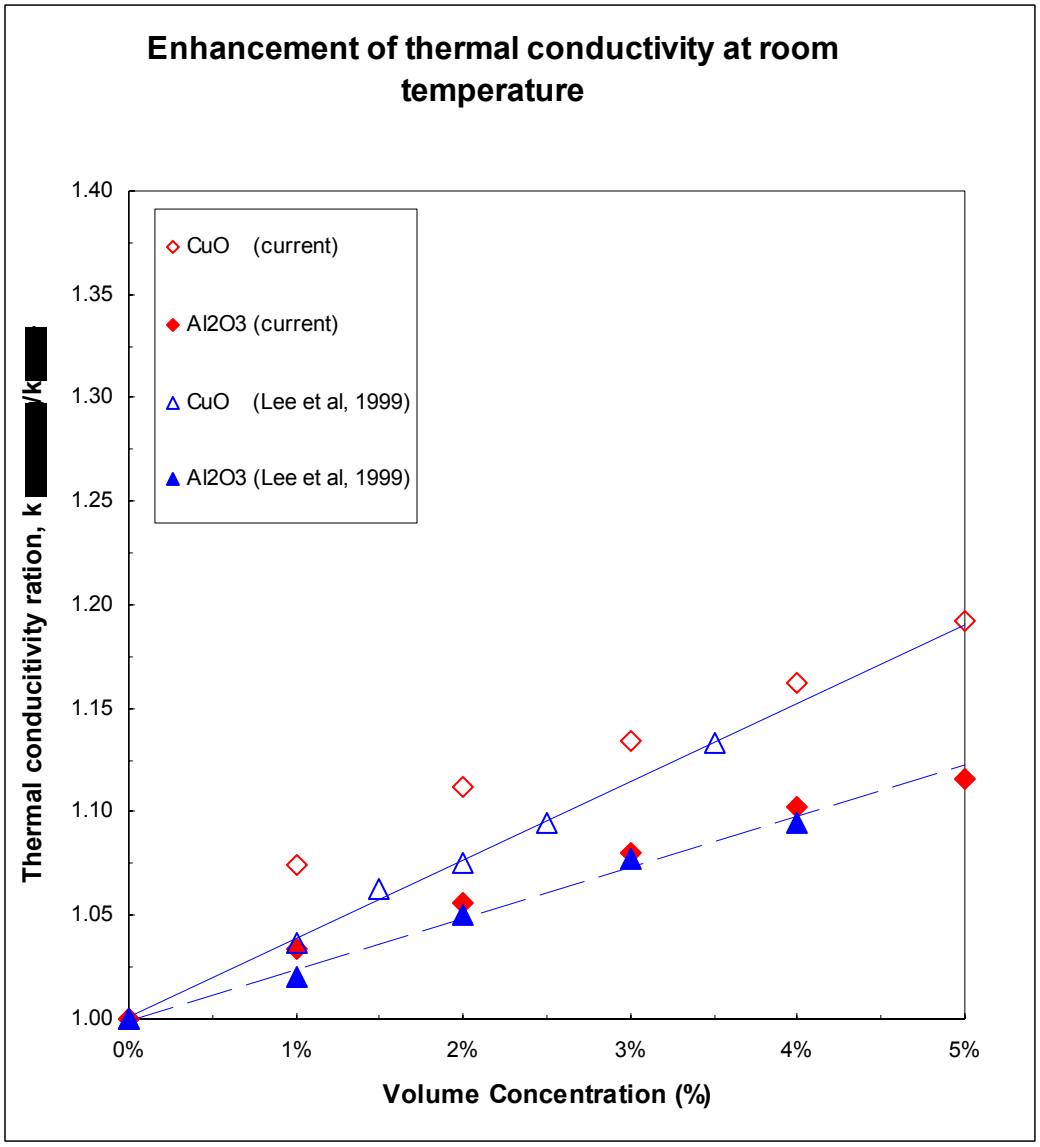

Figure A-3. Enhanced thermal conductivity with increasing volume fraction of nanoparticles measured at room temperature

Figs. A-4 and A-5 present the effects of nanofluidic temperature on the thermal conductivity. The thermal conductivities of nanofluids increase with increasing temperature, which is persistent with the previous finding by Das et al (2003).

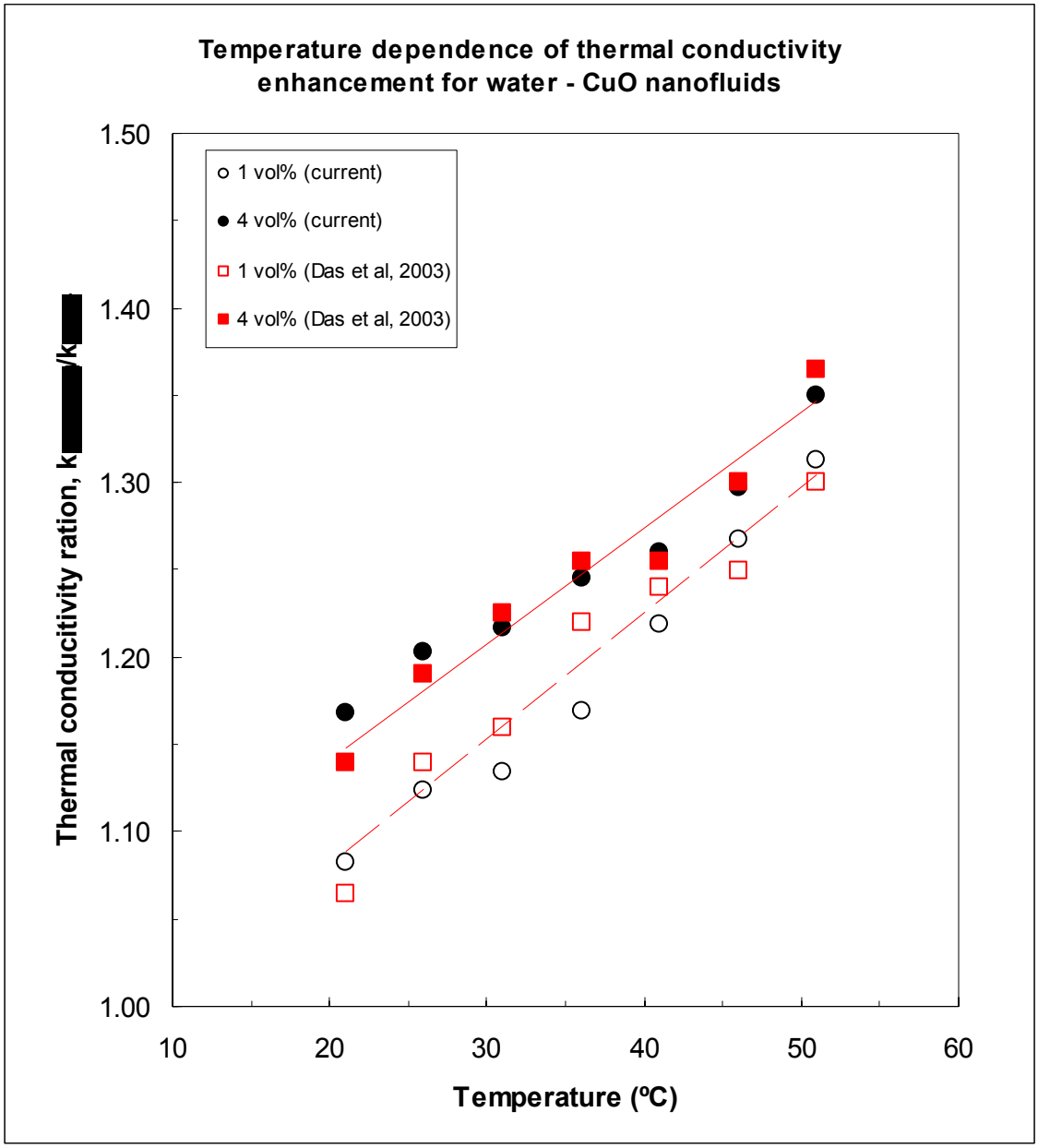

Figure A-4. Temperature dependence of thermal conductivity for water-CuO nanofluids at two different volume fractions.

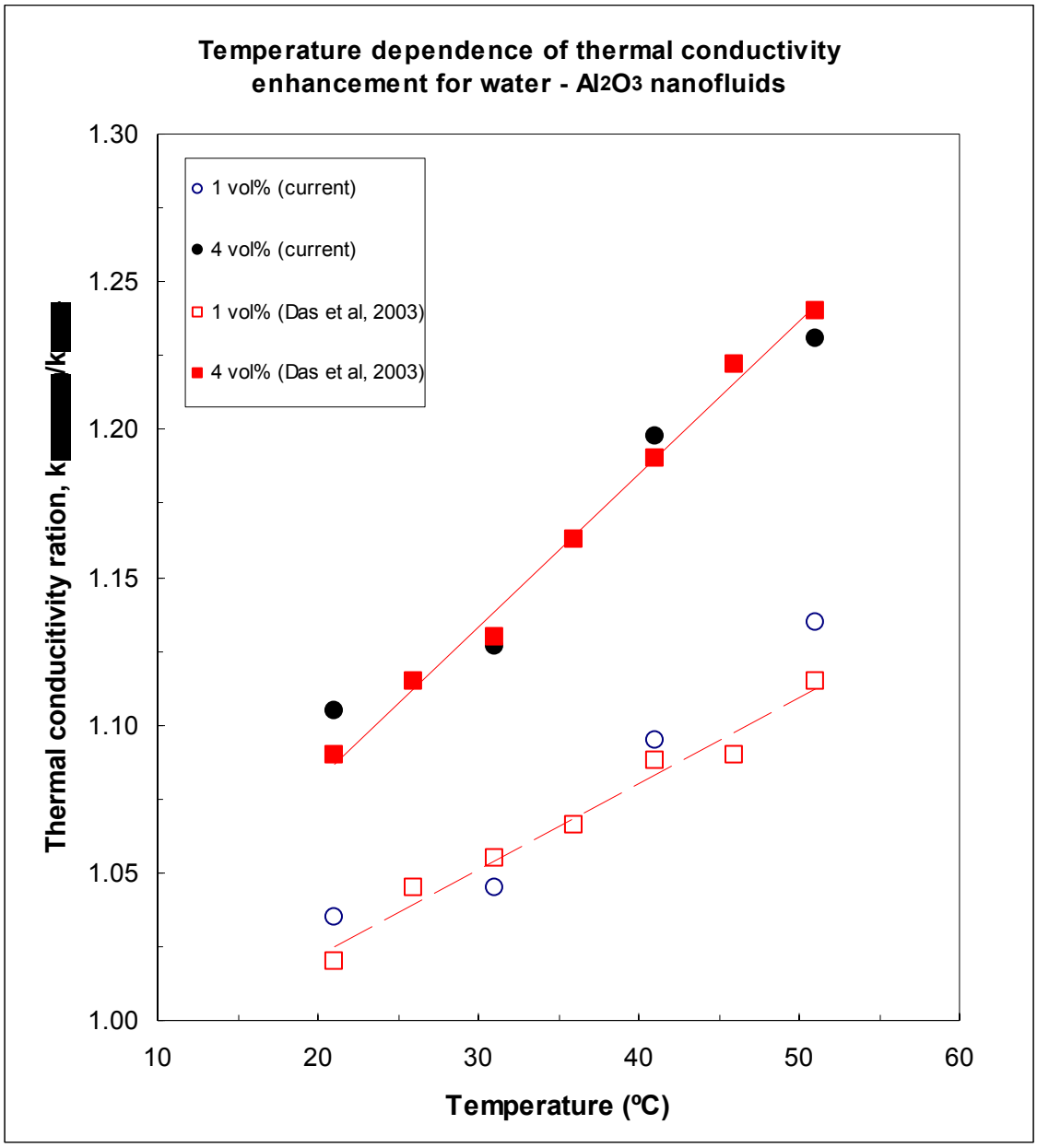

Figure A-5. Temperature dependence of thermal conductivity for water-Al_2O_3 nanofluids at two different volume concentrations.

Appendix 2. Effect of Surfactant on Thermal Conductivity

The second experiment was conducted to examine the effect of surfactants on the thermal conductivity for nanofluids at room temperature. Figure 6 shows that addition of the surfactant substantial reduces the conductivity by more than 30 % from that of nanofluid with no surfactant added.

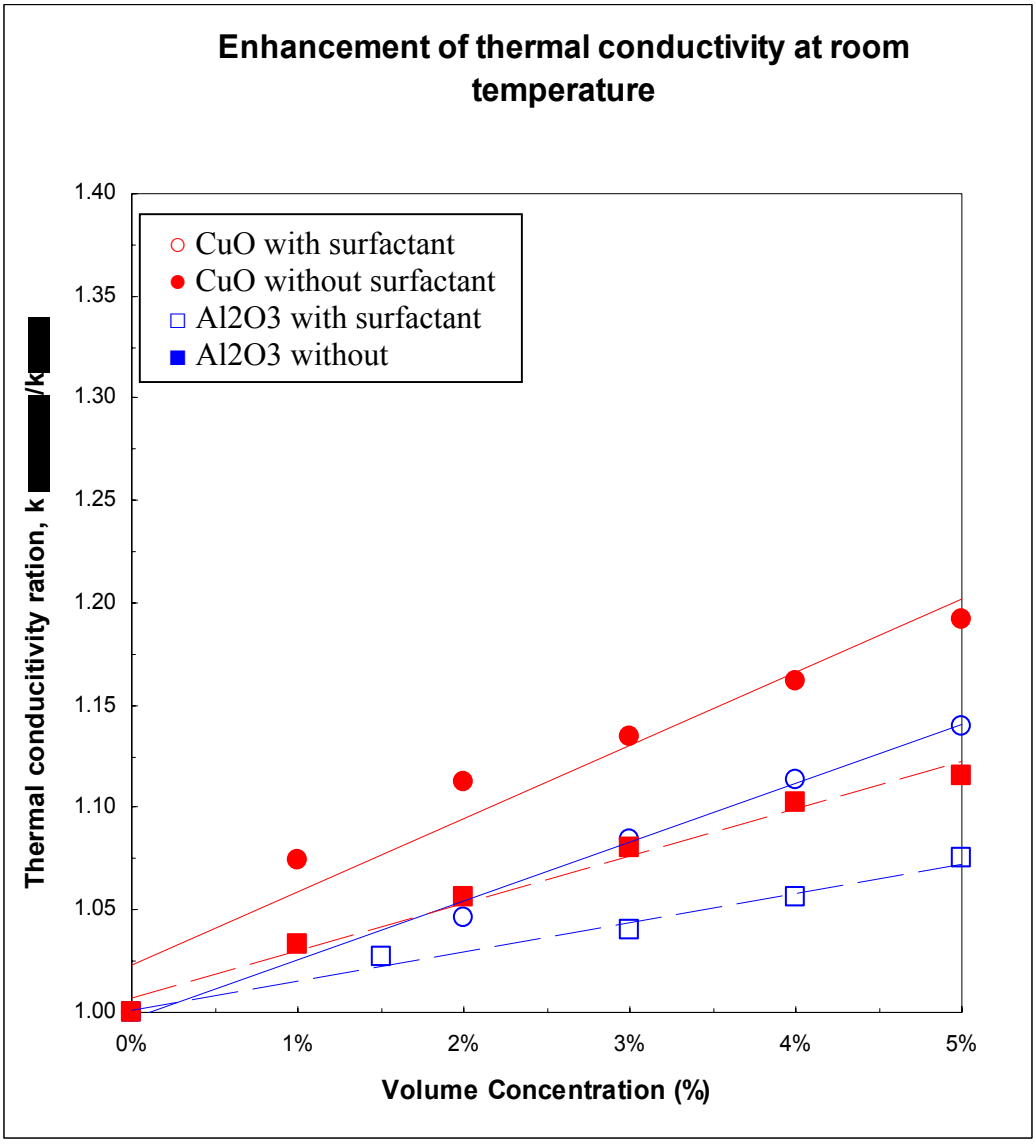

Figure A-6. Enhanced thermal conductivity with/without surfactant at room temperature for both CuO and Al_2O_3 nanofluids

Figures 7 and 8 show the effect of surfactant on conductivity for CuO and Al_2O_3 nanofluids, respectively, at various temperatures. The aforementioned surfactant effect of reducing conductivity is persistent for the tested range of temperatures from 20 to 50°C.

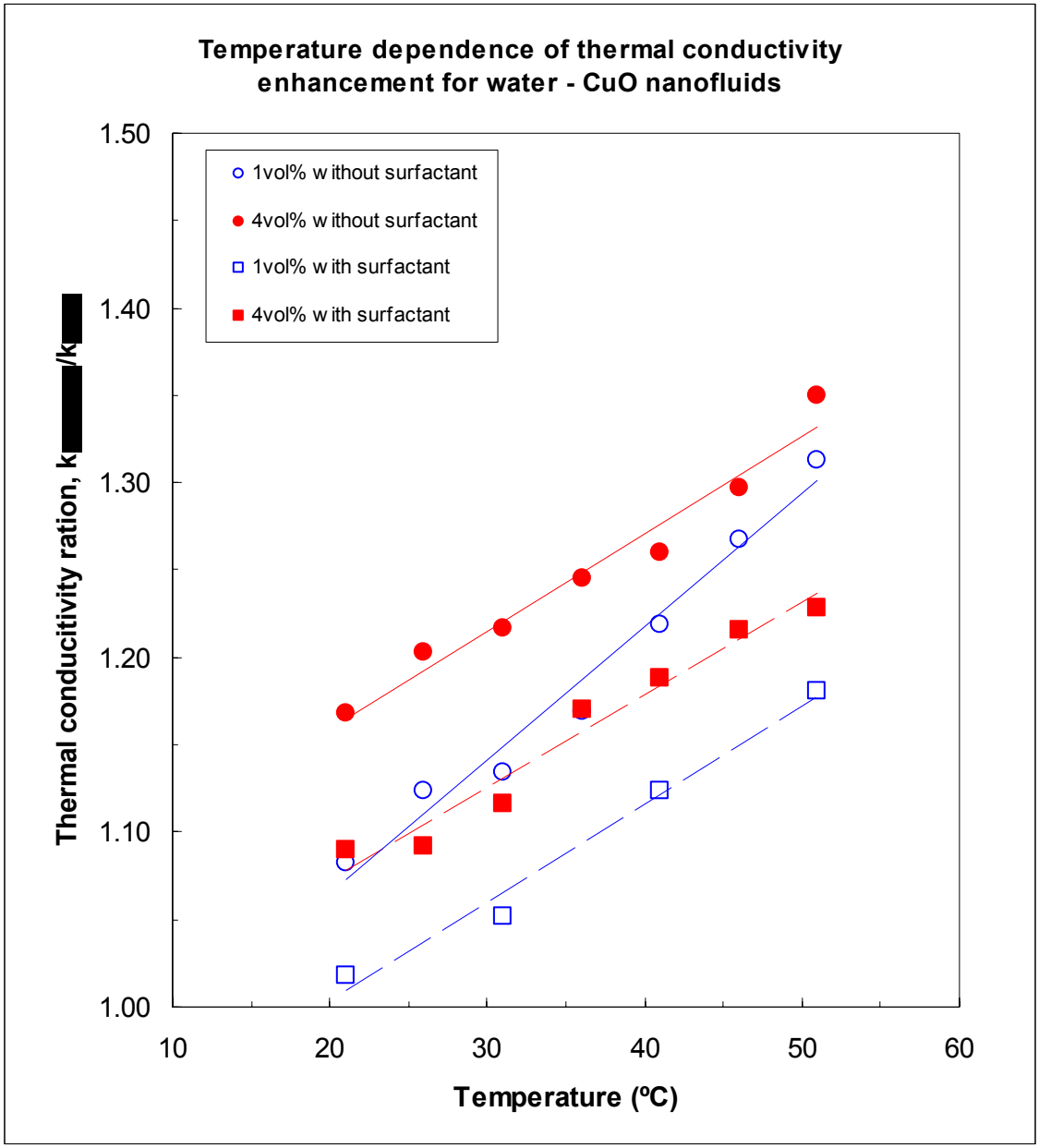

Figure A-7. Temperature dependence of thermal conductivity enhancement with and without surfactant for water-CuO nanofluids

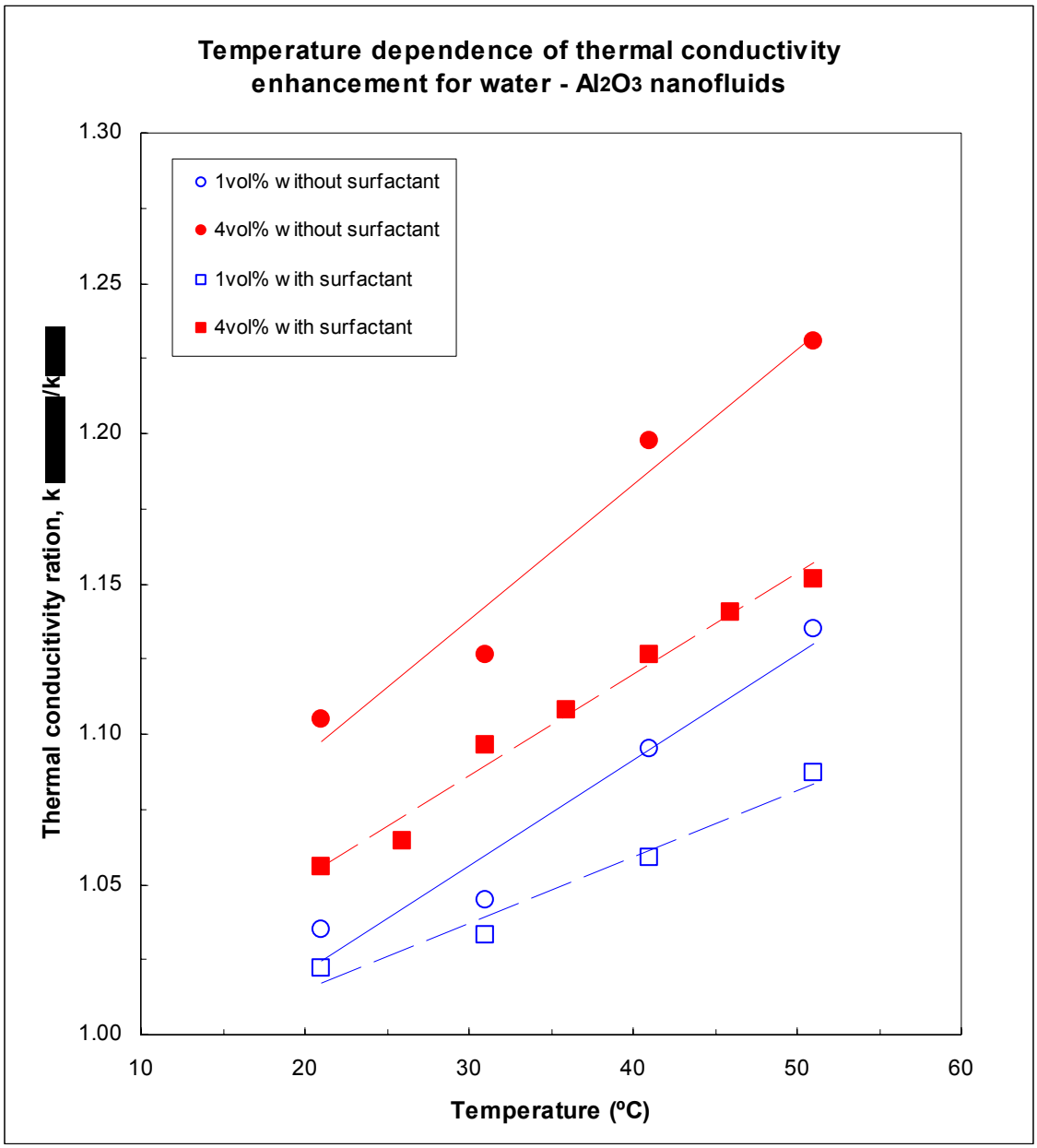

Figure A-8. Temperature dependence of thermal conductivity enhancement with and without surfactant for water-Al_2O_3 nanofluids

Appendix 3. Visualization of Brownian Motion of Nanoparticles

Using wide-field optical microscopy (Olympus BX-61 base and a 60X oil immersion objective with 1.45NA), the Brownian motions of nanoparticles in nanofluids are imaged for PIV analysis and the effect of surfactants on the nanofluidic thermal conductivity will be examined. The experimental setup shown in Fig. 9 includes the mercury lamp illumination and 1024 x 1024 pixel resolution CCD camera at 30 fps recording speed.

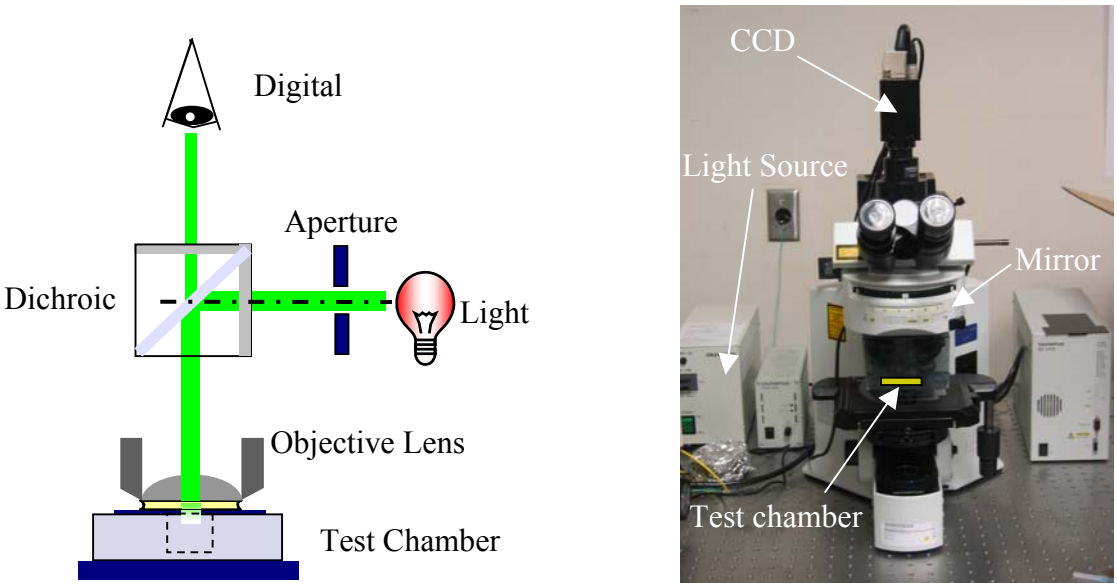

Figure A-9. Experimental setup for visualization of Brownian motions of suspended nanoparticles

By using the 60X objective lens, the recorded image is equivalent to 110.08 μm x 110.08 μm in the test field dimension. The images shown in Fig. 10 are typical single frame images obtained from continually recorded images at 30 fps taken for CuO and Al_2O_3 with and without surfactant added.

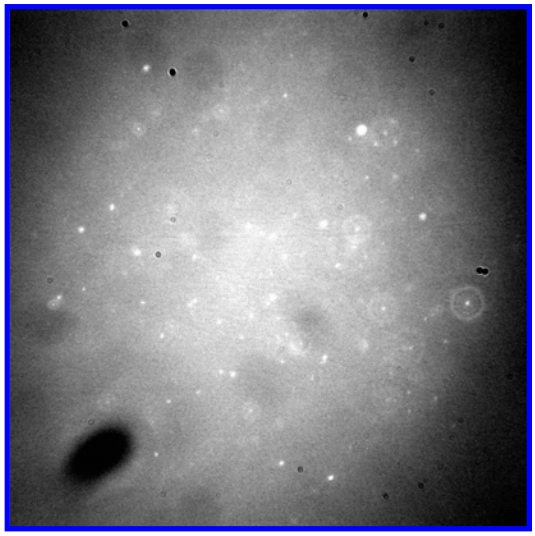

(a) Al_2O_3 without surfactant

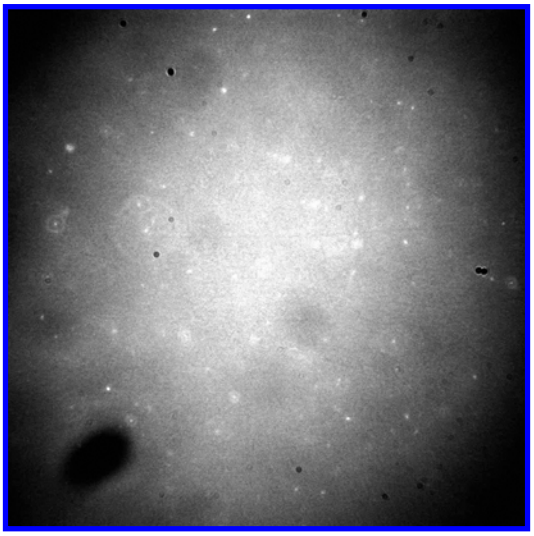

(b) Al_2O_3 with surfactant

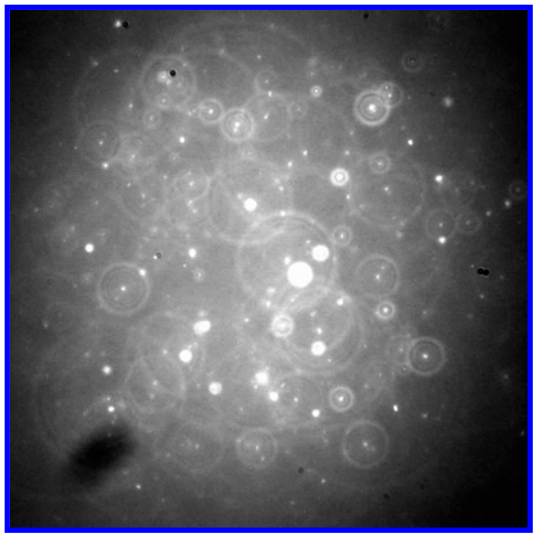

(c) CuO without surfactant

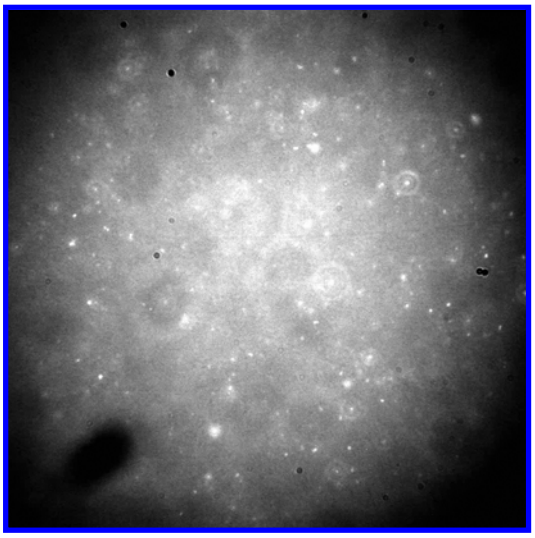

(d) CuO with surfactant

Figure A-10. Microscopic Images of Brownian motions of nanoparticles in nanofluids with and without surfactant

Appendix 4. The accepted manuscript for publication in Experiments in Fluids

---

Near-Wall Hindered Brownian Diffusion of Nanoparticles Examined By Three-Dimensional Ratiometric Total Internal Reflection Fluorescence Microscopy (3D R-TIRFM)

K. D. Kihm[6,7], A. Banerjee[8], C. K. Choi[7], T. Takagi[9]

Abstract A three-dimensional nanoparticle tracking technique using the Ratiometric Total Internal Reflection Fluorescence Microscopy (R-TIRFM) is presented to experimentally examine the classic theory on the near-wall hindered Brownian diffusive motion. An evanescent wave field from the total internal reflection of a 488-nm bandwidth of an argon-ion laser is used to provide a thin illumination field of an order of a few hundred nanometers from the wall. Fluorescence-coated polystyrene spheres of 200±20 nm diameter (SG = 1.05) are used as tracers and a novel ratiometric analysis of their images allows the determination of fully three-dimensional particle locations and velocities. The experimental results show good agreement with the lateral hindrance theory, but show discrepancies from the normal hindrance theory. It is conjectured that the discrepancies can be attributed to the additional hindering effects, including electrostatic and electro-osmotic interactions between the negatively charged tracer particles and the glass surface.

1. Introduction

Single molecule detection techniques (SMD) to visualize the dynamic behavior and reaction kinetics of individual molecules in living cells have recently attracted a great deal of attention (Xie, 2001; Weiss, 2000). The rapid development and progress of SMD techniques have ushered in a revolution in biological research. It is known that the reaction of biological molecules is generally stochastic. Thus, even if the reactions of bio-molecules are initiated at the same time, they cannot be precisely predicted without carefully tracking them (Ishijima and Yanagida, 2001). However, there are certain optical issues associated with the detection and subsequent tracking of single molecules. The size of individual molecules is on the order of nano-meters and they are too small to be visualized by conventional optical microscopy. To overcome this problem, bio-molecules are labeled by fluorescence dyes and visualized using fluorescence microscopy.

[6] Corresponding author, Tel. (865) 974-5292, E-mail: kkihm@utk.edu
[7] Micro/Nano-Scale Fluidics and Energy Transport Laboratory, Department of Mechanical, Aerospace and Biomedical Engineering, University of Tennessee, Knoxville, TN 37996-2210.
[8] Department of Mechanical Engineering, Texas A&M University, College Station, TX 77843-3123
[9] Department of Electrical Engineering, Kushiro National College of Technology, Kushiro, Japan.

The non-invasive nature of the fluorophores associated with the high sensitivity and contrast has made fluorescence microscopy a prominent tool in modern cell biology (Lange *et al*, 2001). However, a significant drawback of light microscopy is dictated by the laws of diffraction. The limit of resolution that can be reached by optical techniques is directly proportional to the wavelength of incident light (Hecht, 2002). This diffraction limit originates from the fact that it is impossible to focus a beam of light to a spot smaller than approximately its wavelength. The challenge to break this diffraction limit has led to the development of several novel imaging techniques. One of them, Total Internal Reflection Fluorescence Microscopy (TIRFM), uses an electromagnetic field called the 'evanescent field' to excite the fluorophores within several hundred nanometers from the interface (Axelrod *et al.,* 1992). This method provides a significant improvement for near field illumination compared to differential interference contrast (Inoue, 1987), confocal microscopy (Pawley, 1995), theta microscopy (Stelzer and Lindek, 1994) or multi-photon microscopy (Denk *et al*., 1990). TIRFM has been a popular technique for both *in vitro* and *in vivo* single molecule detection (Ishijima and Yanagida, 2001; Sako *et al.*, 2000).

The fundamental concept of TIRFM is simple, requiring only an excitation light beam traveling at a high incident angle from the denser medium to the rarer medium (Axelrod *et al*., 1984). At an angle greater than the critical angle, rather than passing through and refracting in accordance with Snell's Law, the beam of light is totally reflected from the glass/water interface (Hecht, 2002). However, the requirements for the momentum and energy boundary conditions at the interface necessitate the existence of a very thin electromagnetic field of an order of a few hundred nanometers in the rarer medium (Goos and Hanchen, 1947). This leakage of electro-magnetic field, popularly called the evanescent wave or field, undergoes exponential intensity decay with increasing distance from the surface (Born and Wolf, 1980). Such a narrow and optically defined excitation depth is considered as the most effective way to overcome the background noise problem that is often the biggest problem in single molecule imaging (Sako and Yanigida, 2003).

Very recently, Zettner and Yoda (2003) proposed seemingly the first microfluidic application of TIRFM to measure the near-wall flow fields for a rotating Couette flow. Their TIRFM system used a prism to provide a total internal reflection and the measuring field was illuminated with a higher order evanescent wave field. The reduced illumination intensity of the higher order field and the astray rays from the multiple reflections resulted in somewhat blurry images, and thus, an elaborate background subtraction was necessary before attempting quantifications of their images for the flow vector field. Shortly after that, the use of a special TIRF objective lens was presented to measure the Brownian motion under various flow shear conditions (Jin *et al.*, 2003). This study is a nice example to use TIRFM for study of near-wall particle diffusive motion, however, the measurement scope is limited to two-dimensional in nature, similar to the former study. The out of plane examination of the Brownian motion will be needed to further investigate the near-wall hindered diffusion that is inherently three-dimensional.

The current paper presents a novel three-dimensional particle tracking technique development using a ratiometric TIRFM principle (Rohrbach *et al.,* 2000**;** Banerjee *et al.,* 2003) in the extremely near region to a solid surface. A three-dimensional reconstruction of the particle position is performed by combining a two-dimensional planar (x-y) tracking of the lateral movement of the particles and the ratiometric TIRFM to determine the line-of-sight (z) movement. This ratiometric technique can now be called R-TIRFM imaging technique. A robust Neural Network model to track particle pairs has been also developed to simultaneously measure

three-dimensional Brownian diffusive motions of nanoparticles. The experimental findings clearly evidence the theory of near-wall hindered diffusion particularly within sub-micron ranges from the solid wall surface. The measurement results are compared with the Stokes flow model for diffusion (Einstein, 1905) and the hindered diffusion theories (Goldman *et al.*, 1967**;** Brenner, 1961**;** Kim and Karrila, 1991). The present study is considered as the first attempt, to the authors' knowledge, to experimentally validate and examine the near-wall hindered diffusion theory fully in three-dimensional mode[10].

2.1 Evanescent Wave Theory

As the ray incident angle, measured relative to the normal, increases, it reaches the *critical incident angle*: $\theta_c = \sin^{-1}\left(n_t / n_i\right)$**,** at which the angle of refraction is 90º. At angles larger than the critical angle, light is completely reflected at the interface, i.e., the total internal reflection. This description, however, is only true from the macroscale point-of-view. From the microscale point-of-view, a portion of the incident light penetrates through the interface into the external medium, and propagates parallel to the surface in the plane of incidence creating an electromagnetic field in the liquid (the external medium) adjacent to the interface. This field, termed as the *evanescent field*, is capable of exciting fluorophores residing in the immediate region extremely near the interface.

The evanescent wave intensity I decays exponentially with the normal distance z measured from the interface located at $z = 0$ (Hecht, 2002).

$$I(z) = I_0 \exp\left(-\frac{z}{z_p}\right) \qquad (1)$$

where I_0 is the incident light intensity at the interface and the penetration depth at $I / I_o = e^{-1}$ is determined as

$$z_p = \frac{\lambda_0}{4\pi}\left(n_i^2 \sin^2\theta - n_t^2\right)^{-\frac{1}{2}} \qquad (2)$$

Figure 1 shows the evanescent wave field intensity variation, based on Eqs. (1) and (2), with increasing depth z measured from the glass ($n_i = 1.515$) – water ($n_t = 1.33$) interface for different incident angles θ. With increasing θ the field intensity decays faster and the penetration depth z_p is smaller[11]. Note that for all incident angles, 10% intensity is reached within 300-nm range from the interface.

2.2 High NA Objective based TIRFM System

Traditionally, two different configurations of TIRFM are popular (Axelrod, 1984). The first set up with a prism can be readily achieved and requires only the microscope, prism, and laser. This setup requires that the specimen be positioned between the prism and the microscope objective and the higher order evanescent wave field must be used due to the geometrical

[10] Hosoda *et al.* (1998) have shown that the near-wall Brownian motion is found to be anisotropic with respect to the directions parallel and perpendicular to the interface using evanescent wave microscopy. Spectroscopic analysis was conducted allowing a wide range of wave number, by varying the incident ray angle, and the resulting autocorrelation function of the image intensity showed an evidence of the anisotropy. However, the scope of their work is far from being comprehensive in that no quantitative measurements of the near-wall hindered diffusion motion have been conducted and compared with the existing theories.

[11] Refer to Fig. A-1 in Appendix for the calculation uncertainties in determining the penetration depth.

constraint, which substantially weakens the field intensity after repeated internal reflection modes. In addition, because of the repeated reflection modes, more strayed rays are rendered resulting in images with low signal-to-noise ratios.

The second and presently preferred setup implements the laser to be illuminated through an inverted microscope, and greatly benefits from a special TIRF objective lens with a numerical aperture (NA) greater than 1.4. Figure 2-a shows the schematic illustration of the objective lens-based TIRFM system where an Olympus Plan APO 60X oil immersed TIRF lens with a NA of 1.45 is used. The experimental setup consists of an inverted microscope (IX-50, Olympus Inc.), a 200-mW CW argon-ion laser (tuned at 488-nm, Laser Physics Inc.), a frame grabber board (QED Imaging Inc.), and particle tracking analysis software, which has been developed at the authors' Micro/Nano-Scale Fluidics and Heat Transport Laboratory [http://go.to/microlab]. The upper outlet port of the microscope is connected to the CCD camera[12]. Tested nanoparticles are yellow-green (505 nm/515 nm) carboxylate coated fluorescent micro-sphere beads[13] of 200-nm (±20-nm variance) diameter, which have a specific gravity of 1.05 and carry weekly negative charges because of their $COOH^-$ group attached to carboxylate (Molecular Probes Inc.). The specimen is placed on the upper surface of the 170-μm thick glass slip, which is viewed from the below.

The critical angle for the lens with total internal reflection at a water-glass interface is $\theta_{critical} = \sin^{-1}(1.33/1.515) = 61.38°$. For an oil-based objective with 1.45 NA, the maximum angle of passage of light is $\sin^{-1}(NA/n_i) = \sin^{-1}(1.45/1.515) = 73.15°$ (Hecht, 2002). The present optical configuration allows that the incident angles can be varied from $\theta_i = 62°$ (z_p = 272 nm) to 68° (z_p = 86 nm)[14]. As schematically illustrated in Fig. 2-b, the angle of incidence is determined by using a transfer function $R = fn\sin\theta_i$ involving the off-center location of the laser beam in the optical pathway of the microscope R, the focal length of the TIRFM objective f, and the refractive index n of the cover glass or equivalently of the index-matching oil (see Appendix A.1 for related discussions).

Figure 3 provides a comparison between the direct and the evanescent wave illuminated images. For non-TIRFM image with $\theta_i = 60° < \theta_{critical}$ (Fig. 3-a), light scattering from out of focus particles causes significant background noise. For the TIRFM image with $\theta_i = 65°$, the

---

[12] Model UP-1830 UNIQ with 1024 × 1024 pixel CCD elements and each pixel element dimension of 6.45μm × 6.45μm. The camera operates at 30 frames per second with minimum illumination of 0.04 lux and S/N ratio better than 58-dB. A certain level of image smearing, because of the finite exposure time, is inevitable and may tend to render the image intensity, however, this does not render the ratiometric measurements since the maximum intensity is considered for all particle images including the reference one. Note that the measured particle location is referred to its closest pole from the solid surface, i.e., the brightest point (refer to Section 2.3).

[13] The dye particles are believed to be free from the "photo-bleaching" effect that can render the dye to unable to fluoresce after excessively exposed to high intensity pumping light. As per specifications of Molecular Probes, the aqueous suspensions of fluorescent beads do not fade noticeably when illuminated by an intense 250-watt xenon-arc lamp for 30 minutes. Since the current experiment uses approximately 40-mW illumination at 488-nm band from the 200-mW nominal laser for the total exposure time of up to four (4) seconds, any errors associated with photo-bleaching should be negligibly minimal.

[14] The high-NA objective based TIRFM systems adjusts the incident angle using a fiber optic laser guide attached to a precision positioning system traveling along the barrel axis.
[http://www.olympusmicro.com/primer/java/tirf/tirfalign/index.html]

signal-to-noise ratio is substantially improved because of the discrete illumination field specified by the penetration depth of z_p = 114 nm (Fig. 3-b).

2.3 Ratiometric Imaging Analysis

The detected fluorescence signal at an arbitrary test field point (x, y) integrated in the line-of-sight direction z through the microscope objective (Fig. 4), $F(x, y; z_p)$ can be described as (Rohrbach, 2000):

$$F(x,y;z_p) = \varepsilon \cdot I_0(x,y;z_p) \cdot \int_0^\infty \left[Q(z) \cdot P_D(z)\right] \cdot C(x,y,z) e^{-\frac{z}{z_p}} dz \qquad (3)$$

where ε defines the quantum efficiency of fluorescent particles and of a CCD camera, which is assumed to be equal for all depth-wise locations z, and $I_0(x, y; z_p)$ is the illumination intensity at the coverslip glass-water interface. The integration in the z-direction implies that the signal detected by a CCD represents the line-of-sight integrated image via the microscope objective. The presence of a dielectric interface (the coverslip in this case) significantly alters the probability of detecting the emitted fluorophores. This effect is traditionally expressed by the collection efficiency $Q(z)$ of the objective lens. The collection efficiency is defined as the collected power to the total power dissipated by a dipole, and its detailed mathematical formulations have been attempted by various authors (Burghardt and Thompson, 1984; Hellen and Axelrod, 1986). The detection probability P_D is set equal to 1 since it is expected to be constant over the evanescent wave field. Lastly, $C(x,y,z)$ denotes the three-dimensional fluorophore distribution that is defined discretely as:

$$\begin{aligned} C(x,y,z) &= c \qquad if \quad \sqrt{x^2+y^2+(z-h)^2} \le R \\ &= 0 \qquad if \quad \sqrt{x^2+y^2+(z-h)^2} > R \end{aligned} \qquad (4)$$

where R is the fluorescent particle radius.

After substituting Eq. (4) into Eq. (3), and then performing substantial mathematical manipulations including a pertinent three-dimensional integration, with an assumption of $Q(z)$ = 1.0, the normalized intensity detected by a CCD for a fluorescent particle of radius R located at h from the interface (Fig. 4) is expressed as

$$I_N(h,R,c) = 4\pi\, c\, z_p^3 \left[\left(\frac{R}{z_p}\right)\cosh\left(\frac{R}{z_p}\right) - \sinh\left(\frac{R}{z_p}\right)\right] \cdot e^{-\frac{h}{z_p}} \qquad (5)$$

Although Eq. (5), in principle, can determine the particle location (h) by measuring I_N under a specified penetration depth (z_p), the fluorescence concentration function c is difficult to measure and usually not accurately known. By taking the quotient of two recordings, the unknown fluorophore concentration c can be eliminated. Thus, by taking the ratio of I_N from two different particles at two different z-locations, the determination of their relative locations is more appropriate in that the unknown and other experimental uncertainties are cancelled out, i.e.,

$$RI \equiv \frac{I_N^1(h_1,R,c)}{I_N^2(h_2,R,c)} = \exp\left(-\frac{\Delta h}{z_p}\right) \qquad (6)$$

To obtain the relative position Δh of two particles from the Ratiometric Intensity *RI*, care is taken to consider the brightest particle as the reference point[15] of $z = 0$. The relative intensity of other particles, Eq. (6), can determine their depth-wise *z*-locations with respect to the reference zero point. The peak (or maximum) intensity from each particle image is taken for I_N and the resulting ratio of Eq. (6) identifies the nearest point of a particle from the surface.

2.4 Free and Hindered Brownian Diffusive Motions

The observation of random motion was first reported by Jan Ingenhousz (1779) and was subsequently rediscovered and named after the eminent botanist Robert Brown who noted the random motion of pollen particles under a microscope (1828). Albert Einstein used the kinetic theory to derive the diffusion coefficient for such motion in terms of fundamental parameters of the particles and liquid for his well-known doctoral dissertation published in 1905. The classical theory of Einstein applies to suspensions, which are effectively so dilute that each particle is moving alone in an infinite fluid. The particle can be assumed to be a sphere that is large compared to the molecules of the fluid (solvent). Thus, the frictional resistance of the particle can be calculated taking into consideration of ordinary particle hydrodynamics, i.e., given by Stokes Law as

$$F_d = 3\pi\mu d_p u_d \tag{7}$$

and the diffusion coefficient *D* for a dilute suspension of particles as originally defined by Einstein in 1905 as

$$D = \frac{kT}{3\pi\mu d_p} \tag{8}$$

where *k* is Boltzman's constant (1.3805 x 10^{-23} J/K), *T* is the absolute temperature, and μ is the dynamic viscosity of the fluid. Recently, using a simple video microscopy (Salmon *et al*., 2002**;** Nakroshis *et al*., 2003), the elementary one- and two-dimensional Brownian motions have been examined for freely diffusing 1.02-μm polystyrene spheres suspended in water to show the validity of the Einstein relationship and inversely determine the Boltzman's constant.

Being stochastic in nature, the mathematics of Brownian motion is actually deep and subtle and care should be taken to interpret the results. It should be kept in mind that a diffusion equation does not provide information on the particle trajectory (Shlesinger *et al*., 1999). Various authors have erred in attempting to define a constant velocity *v* for the Brownian trajectory by taking the limit $\Delta x/\Delta t$ for small displacement Δx and small time Δt. The proper limit involves forming the diffusion coefficient $D = (\Delta x)^2 / \Delta t$ as both Δx and Δt go to zero. Thus, for a finite time interval, the parameter to be used for defining a random walk pattern should be the mean square displacement (MSD) rather than a misleadingly incorrect attempt to convert the definition of *D* into a physically groundless "Brownian velocity" as $\sqrt{D/\Delta t}$ or its multiplication by a constant.

---

[15] The physical location of the brightest particle may not be exactly at zero at the solid surface; rather it should be at the most probable separation distance. Since both the glass surface and particles are negatively charged, there exists the most probable separation distance, which is equivalent to the minimum potential energy state ensuring the mechanical equilibrium. Thus, $z = 0$ here indicates just a reference point for the relative locations of other less bright particles.

A three-dimensional mean-square displacement (MSD) is referred to random thermal or Brownian diffusivity by the Einstein-Smoluchowski Equation as

$$\langle \Delta r^2 \rangle = \langle \Delta x^2 \rangle + \langle \Delta y^2 \rangle + \langle \Delta z^2 \rangle = 6D\Delta t \qquad (9)$$

where Δt is the time interval for the Brownian process and the operator $\langle \cdot \rangle$ denotes an averaged MSD. For example, $\langle \Delta r^2 \rangle = \sum_i^N \Delta r_i^2 \Big/ N$ and $\langle \Delta y^2 \rangle = \sum_i^N \Delta y_i^2 \Big/ N$ for three-dimensional MSD and y-directional (1-D) MSD, respectively. Note that the mean displacement $\langle \Delta r \rangle$ of the particle vanishes because of the spherical symmetry of random motion and contains no information on D (Deen, 1998).

When the particle is present close to a solid wall, the particle hydrodynamics changes significantly. Stokes Law applies only to a fluid medium that extends to infinity in all directions. This assumption does not strictly hold true as a free surface or a rigid wall forms an external bound to the fluid. Furthermore it has been found that the dynamics of the particles close to the wall becomes significantly non-Gaussian and the average particle displacement differs from the theoretically predicted most probable particle displacement (Schatzel *et al.*, 1992).

The presence of these boundaries at finite distances from the particle necessitates the corrections to the Stokes' resistance formula. Brenner (1961) provided an analytical expression in the form of an infinite series for this correction term. He used a hypothesis of no relative motion at the fluid solid interface. By using an analogy of evanescence of velocity at the plane wall, Brenner refined his boundary conditions and solved the resulting Navier Stokes Equation for a creeping flow to derive the correction parameter ξ for the correction of the diffusion coefficient in the normal direction as

$$\xi^{-1} = \frac{4}{3}\sinh\alpha \cdot \sum_{n=1}^{\infty} \frac{n(n+1)}{(2n-1)(2n+3)} \left[\frac{2\sinh(2n+1)\alpha + (2n+1)\sinh 2\alpha}{4\sinh^2(n+\frac{1}{2})\alpha - (2n+1)^2 \sinh^2 \alpha} - 1 \right] \qquad (10)$$

where α is given as a function of the particle diameter d_p and the elevation h from the interface to the base (the bottom most point) of the sphere:

$$\alpha = \cosh^{-1}\left(\frac{2h + d_p}{d_p} \right) \qquad (11)$$

Now, the "hindered" one-dimensional normal diffusion coefficient $D_\perp$ of a spherical particle at a base distance h from the wall can be written as:

$$D_\perp = \xi \frac{kT}{3\pi\mu d_p} = \xi \cdot D \qquad (12)$$

The findings of Brenner has been supported by a number of authors who have highlighted the need for a correction to the Stokes Law for a particle close to a wall or for the case where there are two or more particles close to each other (Dufresne *et al.,* 2000).

Goldman *et al*. (1967) analyzed the slow viscous motion of the sphere parallel to a plane wall bounding a semi-infinite, quiescent, and viscous fluid and used an asymptotic solution of the Stokes Equation for rotational and translational motion close to the wall. Using an analogy corresponding to a translational lubrication theory, corrected values of tangential forces and

torques on the spherical particle have been evaluated. The resulting correction parameter for the tangential force as a result of the presence of the solid wall is given by

$$\beta^{-1} = \left[1 - \frac{9}{16}\left(\frac{d_p}{d_p + 2h} \right) + \frac{1}{8}\left(\frac{d_p}{d_p + 2h} \right)^3 - \frac{45}{256}\left(\frac{d_p}{d_p + 2h} \right)^4 - \frac{1}{16}\left(\frac{d_p}{d_p + 2h} \right)^5 \right] \quad (13)$$

which is a function of the particle diameter d_p and its elevation h. Thus, the "hindered" tangential diffusion coefficient $D_{//}$ of a spherical particle at a distance h from the wall can be written as:

$$D_{//} = \beta \frac{kT}{3\pi\mu d_p} = \beta D \quad (14)$$

The correction factor for the three-dimensional diffusion coefficient is given as:

$$D_O = \psi D \quad with \quad \psi = \frac{2\beta + \xi}{3} \quad (15)$$

where the arithmetic addition of all three directional components of MSD constructs the total or bulk MSD as shown in Eq. (9). The values of ξ, β, and ψ for a particle diameter of 200 nm and for various elevations up to 1.0-μm, are shown in Fig. 5. When multiple particles are present, particle-to-particle should be carefully examined. However, if the ratio of the separation distance to the particle radii is greater than 10, particle interaction effects can be neglected (Batchelor, 1975). Thus, inter-particle interaction is kept to a minimum in the experiment by taking a volume fraction of 0.001%.

2.5 Neural Network Based 3-D Particle Tracking Algorithm

The novel neural network model finds the relationship among particles between a pair of images (Takagi and Okamoto, 2001). The overall operation of the network model is similar to the competitive learning paradigm (Kohonen *et al.*, 1994). A simple two-layered network model (Okamoto *et al.*, 1995 and 1997) is chosen for analysis (Fig. 6). The first layer of the network is the input layer that corresponds to the p^{th} image. The second layer corresponds to the q^{th} image. The two layers are fully interconnected as seen in Fig. 6(a) and the particles of the first and the second layers are labeled as $P = \{p_1, p_2, \cdots, p_n\}$ and $Q = \{q_1, q_2, \ldots, q_n\}$. The coordinates corresponding to the center of each particle in the first layer is (x_{pn}, y_{pn}), while in the second layer it is given as (x_{qn}, y_{qn}). The distance function between two particles of successive layers is given as:

$$d_{i,j} = \sqrt{\left(x_{pi} - x_{qj}\right)^2 + \left(y_{pi} - y_{qj}\right)^2} \quad (16)$$

where the particle center locations are identified as the centroid of the better defined particle images after being processed using a standard 5x5 pixel Gaussian filtering.

Each interconnection in the network model carries an associated weight value (Fig. 6b) as a measure of the correspondence level between paired particles (Kohonen, 1995). For each pair, the weight function w_{ij} is assigned to have a small initial value such as 0.01, and then updated by a rule as proctored by

$$w_{ij}(t+1) = w_{ij}(t) - \alpha \cdot d_{ij} \cdot w_{ij}(t) \quad (17)$$

where $w_{ij}(t)$ is the weight value between the i-th particle of the first image and the j th particle of the second image and $w_{ij}(t+1)$ is an updated weight value. The momentum coefficient α is a type of relaxation factor to control the optimization speed and accuracy, and the coefficient is usually set to be less than one mostly by trial-and-error. When the value of the weight between particles

is large, the probability as the corresponding particle is high showing optimally minimized inter-particular distance d_{ij}. Once all the normalized weight values become greater than a specified threshold, which is to be set to close to 1.0, the iteration stops and the corresponding particle image pairs are identified to provide the most probable displacement of the particle between the successive images.

3. Results and Discussion

Results are presented for near-wall hindered Brownian diffusive motion measured in two-fold: (1) manual tracking of a single particle, and (2) digital image tracking of multiple particles based on particle paring using the neural network algorithm. An incident angle of 62° is used to create an evanescent field thickness z_p of 272 nm for all the experiments. The incident angle is selected so that the penetration depth is sufficiently larger than the near-wall Brownian displacement predictions[16].

The test particle diameters do not have to be smaller than z_p since only the maximum image intensity, usually corresponding to the closest pole of a particle from the solid surface, is detected and analyzed for R-TIRFM. Cell biologists, surface chemists, and colloid scientists have successfully used evanescent wave microscopy to study motion of cells and colloids of size ranges up to 10 μm (Prieve, 1999**;** Bevan and Prieve, 2000). Rohrbach (2000) also used a 60-nm thick evanescent wave field to measure the location of a spatially fixed 300-nm particle using a similar technique. The current penetration depth of 272-nm should be fairly sufficient to illuminate the 200-nm test particles.

Figure 7 shows manually tracked results for the relative locations of multiple 200-nm particles, as frozen in a single frame, with respect to the brightest particle being the zero reference point in the line-of-sight *z*-direction. The uncertainty of the ray angle adjustment is estimated to be ±0.315° for θ_i = 62° (Appendix A.1). For each particle image, the maximum spot intensity is used to calculate the intensity ratio of Eq. (6) and the measured z-location represents the position of the particle bottom. The measurement uncertainties for the lateral *x*-*y* locations are estimated as ±71.7 nm, simply equivalent to one-half pixel distance in both directions (Appendix A.2). The depth-wise location uncertainty decreases with increasing incident angle because of the similar dependence of the penetration depth uncertainty (Appendix A.3 and A.4). For the ray angle of 62°, the uncertainty of Δh in the z-direction is estimated to be ±29.38 nm[17].

Figure 8 shows manually tracked results of an arbitrarily chosen single particle mapped consecutively up to 67 frames when it disappears beyond the effective visualization depth. As the distance of the particle from the interface increases, the intensity decreases exponentially

---

[16] For d_p = 200-nm, k = 1.38054 × 10-23 J/K, μ = 0.001 $N \cdot s / m$ for water at T = 293 K, the free Brownian diffusivity (Eq. (8)) is given as D = 2.1451 $\mu m^2 / s$ and the averaged square displacement $\langle \Delta z^2 \rangle$ = 2 $D\Delta t$ = 0.142 μm^2 for the time interval of 33-ms of the 30 fps imaging. The average displacement $\langle |\Delta z| \rangle$ can be approximated to $\sqrt{\langle \Delta z^2 \rangle}$ = 377 nm. The near-wall hindered displacement (Fig. 5) will reduce it to about one-half, i.e., $\langle \Delta z \rangle \sim \pm$ 189 nm, which occupies approximately 70% of z_p.

[17] When the ray angle increases to 65°, the uncertainty is noticeably reduced to ±6.85 nm but its penetration depth will not be sufficient to accommodate the pertinent Brownian motion length scale.

until the particle vanishes totally. The particle is assumed to be beyond the effective visualization depth when the difference between its maximum pixel intensity and the surrounding pixel intensity approach within 10%. The anisotropic nature of *x*-*y*-*z* components shown in Fig. 8-b clearly evidences the anisotropic near-wall hindrance in Fig. 5. While the *x*- and *y*-displacement shows virtually no distinction as they should be, the significantly further reduced *z*-displacement evidences the more pronounced hindered Brownian motion in the *z*-direction.

The pixelized data characteristics are inevitable for any CCD imaging with a discrete pixel resolution as the discretization length scales of approximately 200 nm are shown in Figs. 8-a and 8-b. The so-called data discretization can be reduced in two ways: (1) by using a CCD with increased pixel resolution (for example, the use of a 2048x2048 CCD will reduce the discretization length scale into one-half from the current case of a 1024x1024 CCD), or (2) by increasing the image magnification so that the field displacement corresponding to a single pixel can be reduced (for example, a substitution of the current 60X objective by a 100X one, the discretization will be reduced to 62.5%). The first option will be excessively costly and the second option will be more viable, but will substantially reduce the field-of-view size. Since the *z*-location is determined based on the ratiometric principle, Eq. (6), no systematic discretization is apparent other than the gray level discretization of roughly 1/256, which is significantly smaller than that of the *x*-*y* displacements.

Figure 9 shows the dynamic behaviors of the entire population of particles for the total of 90 frames using the neural network based particle tracking algorithm as described in Section 2.5. Figure 9-a presents the lateral displacements that are anisotropic and random on the *x*-*y* plane, and Figs. 9-b and -c present the particle displacements on the normal *x*-*z* and *y*-*z* planes, respectively. The more pronounced reduction of particle displacements in the *z*-direction, in comparison with the lateral displacements in the *x*-*y* plane, is persistent with the theoretical predictions of hindered diffusion in the vicinity of a wall (Fig. 5). Figure 9-d presents vectors of three-dimensional displacements that are substantially quenched in the normal direction to conform to an oval shape.

Both the single particle manual tracking data and the neural network based multiple particle tracking data are then compared with the theoretical predictions and the results are summarized in Table 1. The parameters compared include the Mean Square Displacements (MSD), mean displacements, absolute mean displacements, and elementary ($D_\perp$, $D_{/\!/}$) and bulk (D_o) diffusion coefficients, for 200 nm particles in water at T = 293K and for the measurement time interval of 33 ms. While the theoretical isotropic diffusion coefficient is evaluated as D = 2.1451 $\mu m^2/s$, all other presented theoretical values in Table 1 represent their near-wall hindered ones as shown in Eqs. (12), (14) and (15). Spatially averaged correction coefficients within the penetration depth are used to predict theoretical values of the hindered diffusion coefficients as well as MSD. The measured MSD values of $\langle \Delta x^2 \rangle$ and $\langle \Delta y^2 \rangle$ compare well with the theoretical predictions. However, the measured values of $\langle \Delta z^2 \rangle$ rather substantially underestimate compared to the predictions, and the resulting measured $\langle \Delta r^2 \rangle$ slightly but noticeably deviates from the theory. The theoretical diffusion coefficient $D_{/\!/}$ is calculated based on either of the identical MSD in the *x* and *y* directions while the experimental $D_{/\!/}$ is determined from the average of the measured *x* and *y* MSD values. Their comparison is seen to be in good agreement with each other. The measured normal diffusion coefficient $D_\perp$, however, is seen to be about one-third of the theoretically estimated value.

The z-directional underestimation is persistent and believed to be the result of the physical inadequacy and limitation of the near-wall hindrance theory (Brenner, 1961) for the present experimental conditions. The Brenner's analysis takes into consideration only the hydrodynamic interaction between a single sphere and the wall[18]. The resulting correction coefficient for the normal diffusion, ξ in Eq. (10), does not take into account additional hindering effects such as electrostatic and electro-osmotic forces between them. It is the authors' conjecture that the formation of an electronic double layer (EDL) on the cover glass surface plays a key part here. When the cover glass comes in contact with an aqueous solution, the surface hydrolyzes to form the silanol surface group and the glass surface is negatively charged to SiO^-. The negatively charged glass surface attracts the positive hydrogen ions from the weakly ionized water to form EDL (Probstein 1994). The EDL thickness or the so-called Debye length, ranges from 10 to 100-nm depending on the ionic concentration of the solution (Kim *et al*., 2002). This range is well within the penetration depth z_p and the measured displacements can be altered by the electro-osmotic interactions. Consequently, the negatively charged $COOH^-$ group of the fluorescence tracer particles may be repelled away from the surface, and this can act to significantly hinder the diffusion motion beyond the hydrodynamic hindrance, resulting in substantially lower MSD measurements in the normal direction than the Brenner's theory. It is uncertain, however, whether the pertinent effect is the sole reason for the excessive near-wall hindering or not. Certainly more elaborate future investigation will be necessary to examine this conjecture.

The mean particle displacement $\langle \Delta r \rangle$, as well as $\langle \Delta x \rangle, \langle \Delta y \rangle, \langle \Delta z \rangle$, should be ideally zero because of the spherically symmetric random nature of the Brownian motion. The corresponding experimental data well manifests this random nature showing extremely small values. The measured mean absolute displacements $\left(\langle |\Delta r| \rangle \equiv \sum_i^N |\Delta r|_i \Big/ N \right)$ shows acceptable agreement with the theory for both the single and multiple particle results. Since no theoretical estimation is available, the square root of MSD is used to approximately predict the mean of absolute displacements. The $\langle |\Delta z| \rangle$ measurement shows underestimation that is persistent with the previous discussions.

Finally, a comment should be made regarding the various measurement uncertainties associated with the R-TIRFM system. More detailed discussions are presented in Appendix A. Measurement of I_N by Eq. (5) involves a number of errors because of background noise in the image. The major errors are attributed to the background fluorescence and the lateral scattering of the excitation light by the neighboring particles. These errors are largely eliminated by using a low concentration of the fluorophore in water (0.001% by volume at present) and keeping the penetration depth minimal to improve the image contrast. Another important uncertainty occurs in estimating z_p because of the incident angle uncertainty, and the inaccurate refractive indices of the cover glass, the emersion oil, and the fluorophore solution. Additional errors can be caused by the uncertainty of the surface intensity because of the micro/nano-scale nonuniformities of the laser illumination. Indeed, some illumination nonuniformities are substantial, as demonstrated in

[18] Meiners and Quake (1999) attempted a direct measurement of hydrodynamic interaction between two spherical colloid particles, ranging from 3.1 μm to 9.8 μm, two order-of-magnitudes larger than the present nanoparticles, suspended by optical tweezers in an external potential. However, they measured cross-correlations of only two-dimensional motions of particles without accounting for the near-wall hindrance.

Fig. 3-b. However, most particles are fluctuating locally within the region of fairly uniform illumination intensity so that their images are minimally biased by the observed large-scale spatial nonuniformities. As for the temporal variations in the laser intensity, all experiments were performed after the laser beam was stabilized and fluctuations were within 0.1 mW. Furthermore, the intensity variation during such a relatively short imaging period, a maximum of four (4) seconds, should be negligibly small.

7. Conclusive remarks

A novel three-dimensional ratiometric particle tracking technique has been developed and applied to examine the hindered Brownian diffusion of 200-nm fluorescent particles within the penetration depth of z_p = 272 nm from the interface given at θ_i = 62°. Three-dimensional particle displacements are analyzed using a robust Neural Network Model to identify particle pairs across imaging frames. The technique is likely considered as the first of its kind to tag and track nano-particles in a full three-dimensional way with unprecedented nanometer spatial resolution. The overall measurement uncertainties are estimated as ±71.7 nm both in the *x*- and *y*-direction, and ±29.38 nm in the *z*-direction. The measured Brownian diffusion behavior show fairly impressive agreement with the near-wall hindrance theory in the lateral *x*-*y* plane, but the measured diffusion coefficient in the *z*-direction shows approximately one-third of the theory. Noting that the theory is based on the consideration of the pure hydrodynamic interaction of a single particle with the wall, the authors propose to further examine the near-wall hindrance model by additionally incorporating non-hydrodynamic effects such as electrostatic and electro-osmotic forces that may be prevalent within the penetration depth of the evanescent wave field.

Acknowledgement

The authors wish to thank Mr. Eiji Yokoi of Olympus America Inc. for his technical assistance in setting up the TIRFM system. The authors are grateful to the financial support sponsored partially by the NASA-Fluid Physics Research Program Grant No. NAG 3-2712, and partially by the US-DOE/Argonne National Laboratory Grant No. DE-FG02-04ER46101. The presented technical contents are not necessarily the representative views of NASA, US-DOE or Argonne National Laboratory.

References

Axelrod D; Hellen EH; Fulbright RM (1992) Total Internal reflection fluorescence. In: Lakowicz J (ed) Topics in Fluorescence Spectroscopy: Principles and Applications. Vol.3: Biochemical Applications. Plenum Press, New York, pp 289-343

Axelrod D; Burghardt TP; Thompson NL (1984) Total Internal reflection fluorescence (in biophysics). Annl Rev of Biophys and Bioengg 13: 247-268

Banerjee A; Chon C; Kihm KD (2003) Nanoparticle tracking using TIRFM imaging. 2003 IMECE Photogallery

Batchelor GK (1975) Brownian diffusion of particles with hydrodynamic interaction. J Fl Mech 74: 1-29

Bevan MA; Prieve DC (2000) Hindered diffusion of colloidl particles very near to a wall: revisited. Journal of Chemical Physics 113(3): 1228-1236

Born M; Wolf E (1980) Principles of Optics, 6th edn. Cambridge University Press, Cambridge, pp 47-51

Brown R (1828) A brief account of Microscopical Observations made in the months of June, July and August, 1827, on the particles contained in the pollen of plants; and on the General Existence of Active Molecules in Organic and Inorganic bodies. Phil Mag 4: 161-173

Brenner H (1961) The slow motion of a sphere through a viscous fluid towards a plane surface. Chem Engg Sci 16: 242-251

Burghart TP; Thompson NL (1984) Effects of planar dielectric interfaces on fluorescence emission and detection. Biophys J 46: 729-737

Deen WM (1998) Analysis of Transport Phenomenon. Oxford, New York, pp 59-63

Denk W; Strickler JH; Webb WW (1990) Two photon laser scanning fluorescence microscopy. Science 248: 73-76

Dufresne ER; Squires TM; Brenner MP; Grier DG (2000) Hydrodynamic coupling of two Brownian spheres to a planar surface. Phy Rev Lett 85: 3317-3320

Einstein A (1905) Über die von der molekularkinetischen Theorie der Wärme geforderte Bewegung von in ruhenden Flüssigkeiten suspendierten Teilchen. Ann Phys 17**:** 549

Einstein A (1956) Investigations on the Theory of Brownian Movement. New York

Fox RW; McDonald AT; Pritchard PJ (2004) Introduction to Fluid Mechanics (6^{th} ed.), John Wiley & Sons, Hoboken, 755-761

Goldman AJ; Cox RG; Brenner H (1967) Slow viscous motion of a sphere parallel to a plane-I: Motion through a quiescent fluid. Chem Engg. Sci 22: 637-651

Goos VF; Hanchen H (1947) Ein neuer und fundamentaler Versuch zur Totalreflexion. Ann Physik 1: 333-346

Hecht E (2002) Optics, 4th edn. Addison Wesley, Massachusetts, 124-127

Hellen EH; Axelrod D (1986) Fluorescence emission at dielectric and metal film interfaces. J Opt Soc Am B 4: 337-350

Hosoda M; Sakai K; Takagi K (1998) Measurement of anisotropic Brownian motion near an interface by evanescent light-scattering spectroscopy. Physical Review E 58(5): 6275-6280.

Ingenhousz J (1779) Experiments on vegetables, discovering their great power of purifying the common air in sunshine, and of injuring it in the shade or at night. Excerpts from Marshall H.L; Herbert S. K (1952) A Source Book in Chemistry: 1400-1900

Inoue S (1987) Video Microscopy. Plenum Press, New York

Ishijima A; Yanagida T (2001) Single molecule nanobioscience. Trends in Biochem Sci 26: 438-444

Jin S; Huang P; Park J; Yoo JY; Breuer KS (2003) Near-Surface Velocimetry using Evanescent Wave Illumination. Proceedings of IMECE 2003:55015

Kim MJ; Beskok A; Kihm KD (2002) Electro-osmosis-driven micro-channel flows: a comparative study of microscopic particle image velocimetry measurements and numerical simulations. Exp Fluids 33: 170-180

Kim S; Karrila SJ (1991) Microhydrodynamics: Principles and Selected Applications. Butterworth-Heinemann: Portland

Kline SJ; McClintock FA (1953) Describing uncertainties in single-sample experiments. Mechanical Engineering 75(1): 3-9.

Kohonen T; Kaski S; Lappalainen H (1994) Self-Organization formation of various invariant-features filters in the adaptive subspace SOM. Neural Comp 9:1321-44

Kohonen T (1995) Self-Organizing Maps. Springer-Verlag: Berlin

Lange FD; Cambi A; Huijbens R; Bakker BD; Rensen W; Parajo MG; Van Hulst N; Figor CG (2001) Cell Biology beyond the diffraction limit: near field scanning optical microscopy. J Cell Sci 114: 4153- 4160

Meiners J-C; Quake SR (1999) Direct measurement of hydrodynamic cross correlations between two particles in an external potential. Physical Review Letters 82(10): 2211-2214

Molecular Probes Inc. (2004) Personal Communications

Nakroshis P; Amoroso M; Legere J; Smith C (2003) Measuring Boltzmann's constant using video microscopy of Brownian motion. Amm. J. Phys. 71(6): 568-573.

Okamoto K; Hassan YA; Schmidl WD (1995) New tracking algorithm for particle image velocimetry. Exp Fluids 19: 342-347

Okamoto K; Nishio S; Kobayashi T; Saga T (1997) Standard images for particle imaging velocimetry, Proc. of The Second Int. Workshop on PIV-97-Fukui, Japan: 229-236.

Pawley JB (1995) Handbook of Biological Confocal Microscopy. 2nd Edn. Plenum Press, New York

Prieve DC (1999) Measurement of colloid forces with TIRM. Advances in Colloid and Interface Science 82: 93-125

Probstein RF (1994) Physicochemical Hydrodynamics. John Wiley & Sons Inc, New York

Rohrbach A (2000) Observing Secretory Granules with a Multiangle Evanescent Wave Microscope. Biophy J 78: 2641-2654

Sako Y; Minoghchi S; Uyemura T (2000) Single-molecule imaging of EGFR signaling on the surface of living cells. Nature Cell Bio 2: 168-172

Sako Y; Yanagida T (2003) Single-molecule visualization in cell biology. Img Cell Bio: SS1-SS5

Salmon R; Robbins C; Forinash K (2002) Brownian motion using video capture. Institute of Physics Publishing 23: 1-5.

Schatzel K; Neumann WG; Muller J; Materzok B (1992) Optical Tracking of Brownian Particles. App Opt 31: 770-778

Shlesinger MF; Klafter J; Zumofen G (1999) Above, below and beyond Brownian motion. Am J Phys 67: 1253-1259

Stelzer EHK; Lindek S (1994) Fundamental reduction of the observation volume in far-field light microscopy by detection orthogonal to the illumination axis: confocal theta microscopy. Opt Commun 111: 536-547

Takagi T; Okamoto K (2001) Particle Tracking Velocimetry by Network Model. Proc of PSFVIP-3, published by CD-Rom

Weiss S (2000) Measuring conformational dynamics of bio-molecules by single molecule fluorescence spectroscopy. Nat Struct Bio7: 724-729

Xie S (2001) Single-molecule approach to enzymology. Single Mol 2: 229-236

Zettner CM ; Yoda M (2003) Particle velocity field measurements in a near-wall flow using evanescent wave illumination. Exp Fluids 34: 115-121

Appendix A. Uncertainty Analyses

Experimental uncertainties have been estimated based on a single-sample experiment, where only one measurement is made for each point (Kline and McClintock, 1953). Four pertinent uncertainties are presented: (A-1) uncertainty for incident ray angle θ, (A-2) uncertainty for the lateral (x-y) Brownian displacement measurements Δx or Δy , (A-3) uncertainty for the penetration depth z_p , and (A-4) uncertainty for the z-directional relative displacement Δh .

A.1 Uncertainty for incident ray angle

The evanescent wave rim radius at the back-focal plane of the lens, R [http://www.olympusmicroscopy.com], is given as $R = fn\sin\theta$, where the focal length of the TIRF objective lens f = 3mm and the refractive index of the incident cover glass medium n = 1.515. A measurement function for the incident ray angle is defined as $\sin\theta = R / fn = g(R, f, n)$. The Kline-McClintock analysis (Fox *et al.,* 2004) for uncertainty w_g gives:

$$
\begin{aligned}
w_g &= \pm\left[\left(\frac{\partial g}{\partial R}w_R\right)^2 + \left(\frac{\partial g}{\partial f}w_f\right)^2 + \left(\frac{\partial g}{\partial n}w_n\right)^2\right]^{\frac{1}{2}} \\
&= \pm\left[\left(\frac{w_R}{R}g\right)^2 + \left(-\frac{w_f}{f}g\right)^2 + \left(-\frac{w_n}{n}g\right)^2\right]^{\frac{1}{2}} \\
&= \pm\left[\left(\frac{w_R}{fn}\right)^2 + \left(\frac{w_f\sin\theta}{f}\right)^2 + \left(\frac{w_n\sin\theta}{n}\right)^2\right]^{\frac{1}{2}}
\end{aligned}
\qquad \text{(A-1)}
$$

where w_R, w_f and w_n are the uncertainties associated with the individual parameters of R, f and n. Per the resolution limit provided by Olympus Inc., w_R = ±0.025 mm, and both the focal length uncertainty, w_f, and the refractive index uncertainty, w_n, are assumed negligibly small. For the incident angle of 62°, the resulting uncertainty is calculated as $\boxed{w_\theta = \pm 0.315^\circ}$ after a conversion based on $w_\theta = \sin^{-1}(w_g)$.

A.2 Uncertainty for the lateral (*x*-*y*) Brownian displacement measurements

A reasonable estimate of the measurement uncertainty due to random error is plus or minus half the smallest scale division, equivalent to one pixel, of the CCD. By taking the average pixel displacements as 3, the lateral displacement uncertainty is estimated to $\boxed{w_x = w_y = \pm 0.5\ pixel \sim \pm 71.7\ nm}$.

A.3 Uncertainty for the penetration depth z_p

Considering Eq. (2),

$$z_p = \frac{\lambda_0}{4\pi}\left(n_i^2\sin^2\theta - n_t^2\right)^{-\frac{1}{2}} \qquad (2)$$

the uncertainty equation for z_p is given as:

$$w_{z_p} = \pm\left[\left(\frac{\partial z_p}{\partial \lambda_o} w_{\lambda_0}\right)^2 + \left(\frac{\partial z_p}{\partial n_i} w_{n_i}\right)^2 + \left(\frac{\partial z_p}{\partial n_t} w_{n_t}\right)^2 + \left(\frac{\partial z_p}{\partial \theta} w_\theta\right)^2\right]^{\frac{1}{2}} \qquad \text{(A-2)}$$

where the optical blue filter for the laser beam has a bandwidth of $w_{\lambda_o} = \pm 2nm$, $w_\theta = \pm 0.315^\circ$ (Appendix A.1) and variations of refractive indices are neglected, i.e. $w_{n_i} = w_{n_t} = 0$. The measurement uncertainty of z_p shows significant increase with the incident ray angle θ approaching the critical value of θ_c = 61.38° (Fig. A.1). For example, the penetration depth uncertainty is estimated as $\boxed{w_{z_p} = \pm 4.75\, nm}$ for $\theta = 65^o$, but increases to $\boxed{w_{z_p} = \pm 69.47\, nm}$ for $\theta = 62^o$.

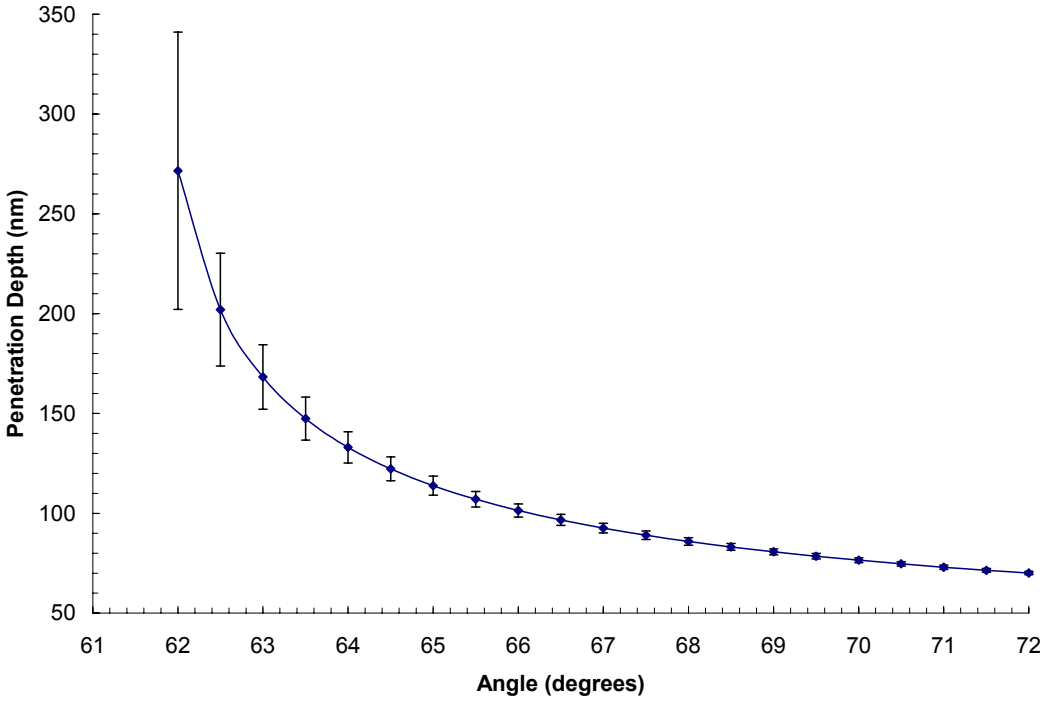

Fig. A-1. Calculated uncertainty for the penetration depth (z_p) for different incident angles (θ) with $\theta_c = 61.38^o$ for the glass (n_i = 1.515) – water (n_t = 1.33) interface

A.4 Uncertainty for the line-of-sight (*z*) Brownian displacement measurements

The uncertainty of Δh can be estimated by applying the uncertainty analysis to the ratiometric intensity relation given in Eq. (6) as:

$$RI \equiv \frac{I_N^1(h_1, R, c)}{I_N^2(h_2, R, c)} = \exp\left(-\frac{\Delta h}{z_p}\right) \qquad (6)$$

or equivalently,

$$\Delta h = -z_p \ln(RI) = z_p[\ln(I_N^2) - \ln(I_N^1)] \qquad \text{(6-a)}$$

Thus the uncertainty equation is obtained as:

$$w_{\Delta h} = \pm\left[\left(\frac{\partial \Delta h}{\partial z_p} w_{z_p}\right)^2 + \left(\frac{\partial \Delta h}{\partial I_N^2} w_{I_N^2}\right)^2 + \left(\frac{\partial \Delta h}{\partial I_N^1} w_{I_N^1}\right)^2\right]^{\frac{1}{2}} \qquad \text{(A-3)}$$

The elementary uncertainties of $w_{I_N^1}$ and $w_{I_N^2}$ may be estimated from the statistical nature of the measured data. A statistical analysis was conducted for the particle tracking date for $\theta_i = 62^\circ$ and the resulting statistical properties are summarized in terms of the pixel gray level as:

Mean Grey Level	165.9404
Standard Error	5.40689
Median	210
Mode	220
Standard Deviation	66.44097
Sample Variance	4414.403
Kurtosis	-1.02024
Skewness	-0.77834
Range	187
Minimum	33
Maximum	220
Sum	25057
Count	151
Largest (1)	220
Smallest (1)	33
Confidence Level (95.0%)	10.6835

Thus, the elementary uncertainties for the image intensities is assumed to be equal to the width of a 95% confidence interval, i.e., $w_{I_N^1} = w_{I_N^2} = \pm 10.6835$ (pixel equivalency), the reference particle image intensity I_N^2 is assumed to have the maximum intensity of 220, and the arbitrary particle image intensity I_N^1 is assumed to have the average intensity of 165.94. Substituting these values in Eq. (A-3), the overall uncertainty for the *z*-location measurements is estimated as $\boxed{w_{\Delta h} = \pm 29.38\, nm}$ for $\theta = 62^\circ$. This R-TIRFM uncertainty also decreases with increasing incident ray angle depicting a similar trend of the penetration depth uncertainty.

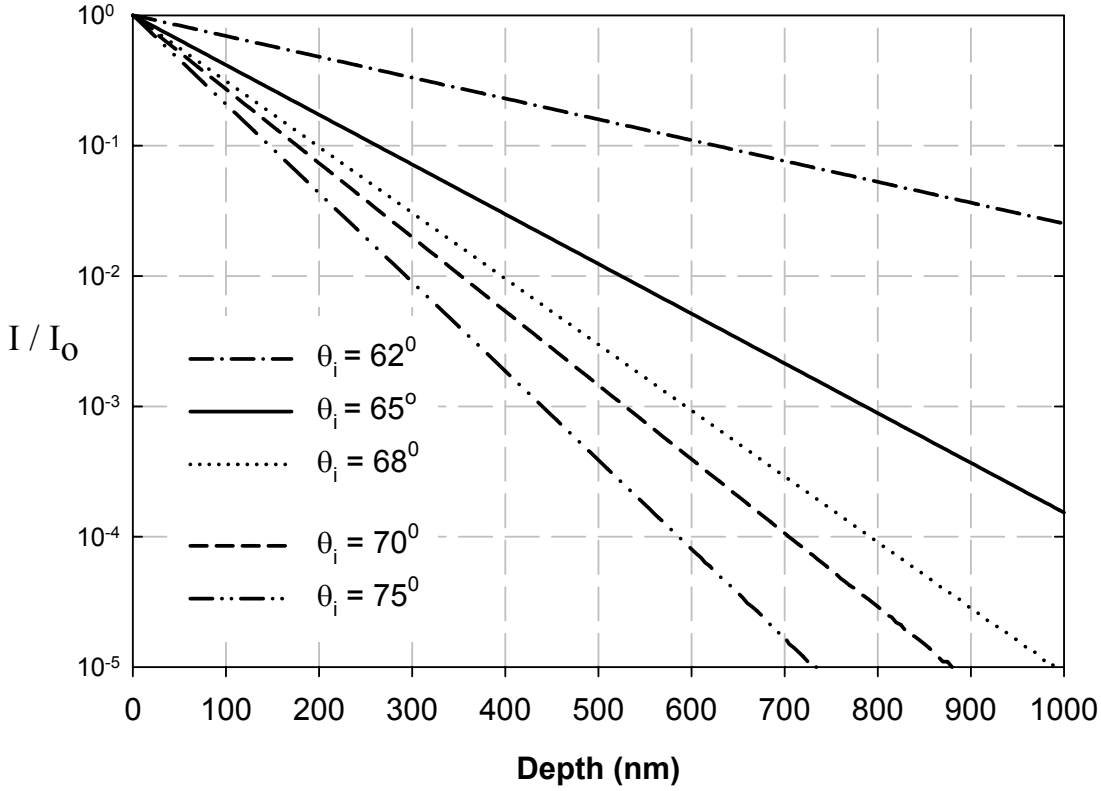

Fig. 1 Calculated evanescent wave field intensity $I(z)/I_o$ for different incident angles θ, with increasing depth z measured from the glass (n_i = 1.515) – water (n_t = 1.33) interface where the incident light intensity is I_o.

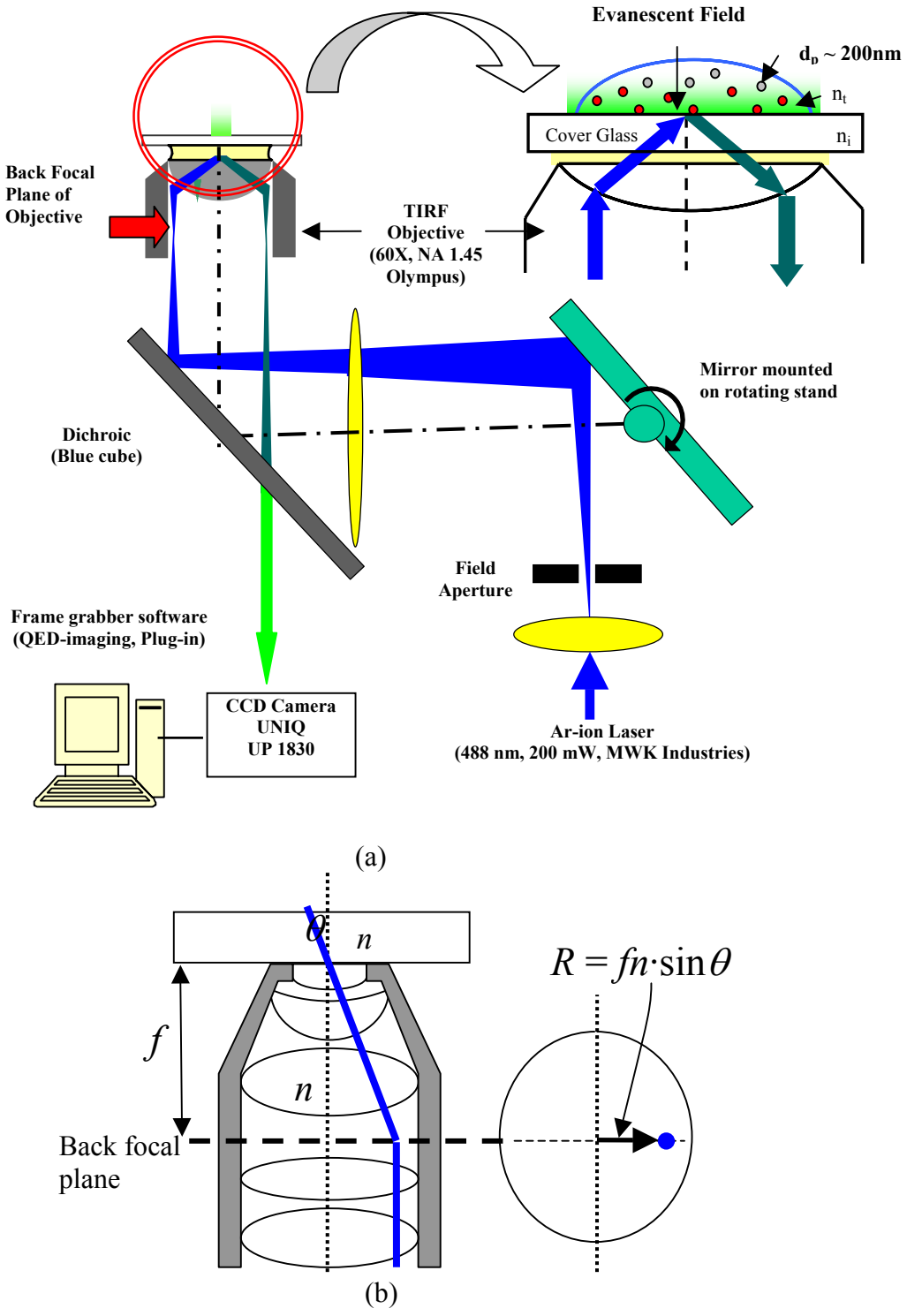

Fig. 2 (a) Schematic illustration of Total Internal Reflection Fluorescence Microscopy (TIRFM) setup with high-NA (oil-immersion type) objective lens, and (b) the illustration of calculation of the beam incident angle using a transfer function for the off-center laser beam location.

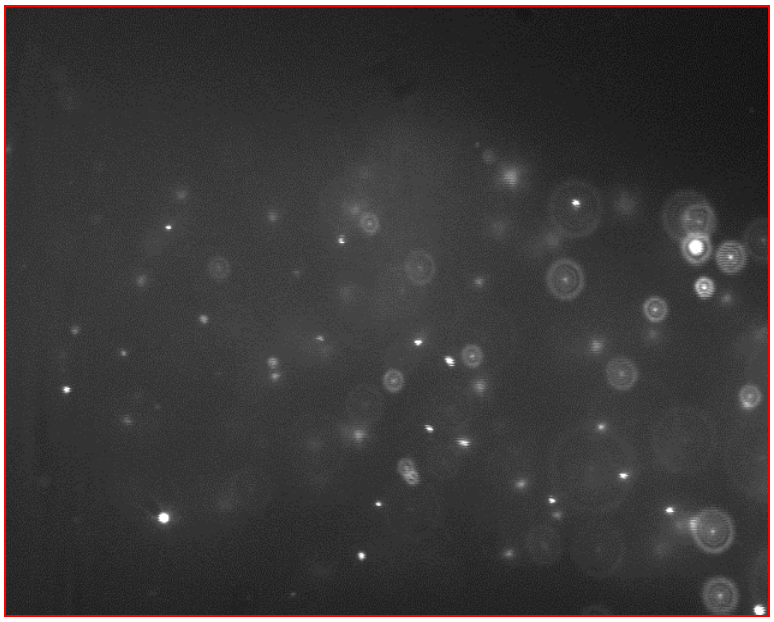

(a) Direct Illumination with $\theta_i = 60°$ ($\theta_{critical} = 61.38°$)

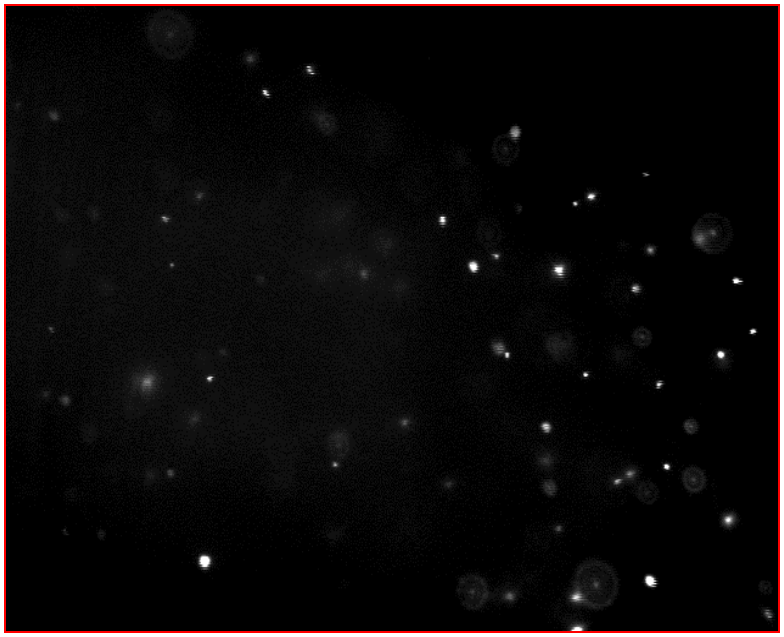

(b) Near Wall TIRFM Image with $\theta_i = 65°$ ($z_p = 114$ nm)

Fig. 3 Comparison of direct illuminated image at an incident angle slightly below the critical angle (a), and evanescent wave illuminated image with an incident angle larger than the critical angle (b).

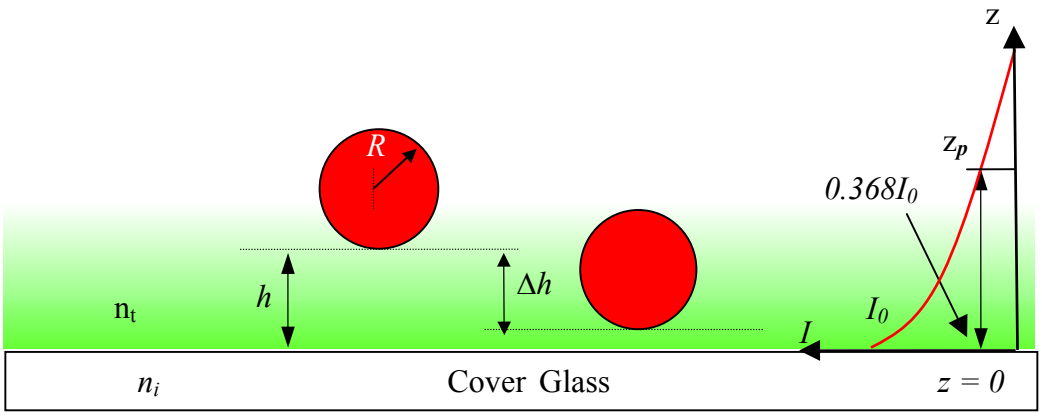

Fig. 4 Two nanoparticles at different *z*-locations schematically illustrating the Ratiometric Total Internal Reflection Fluorescence Microscopic (R-TIRFM) imaging analysis.

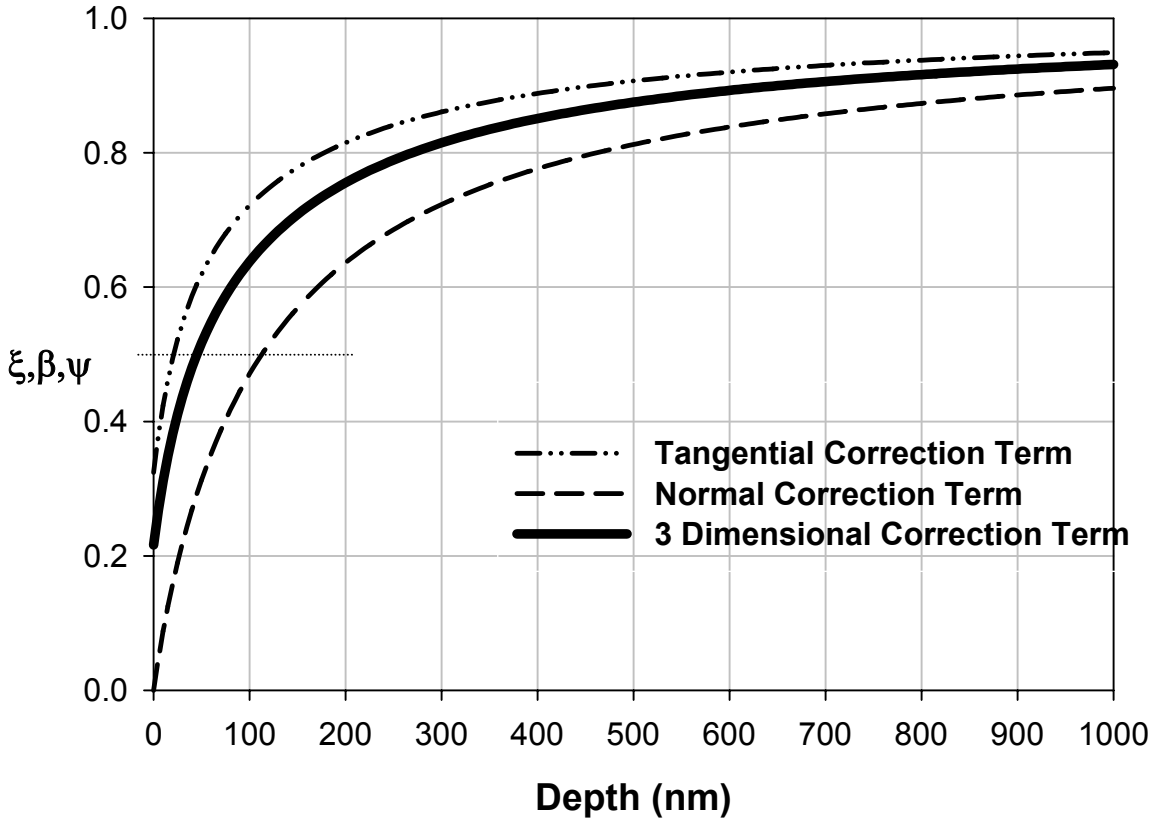

Fig. 5 Correction Factors for Bulk, Normal (Brenner, 1961), and Tangential (Goldman *et al.,* 1967) Diffusion Coefficient as the particle approaches the wall (d_p = 200 nm).

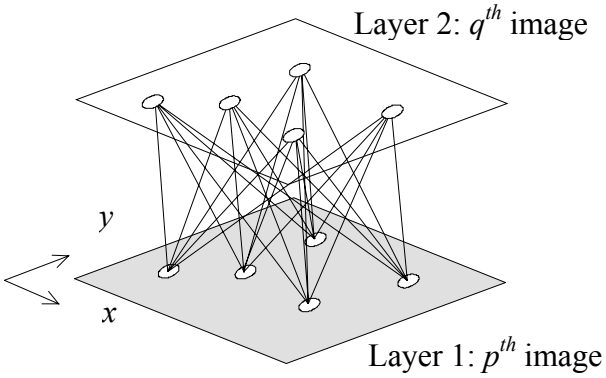

(a)

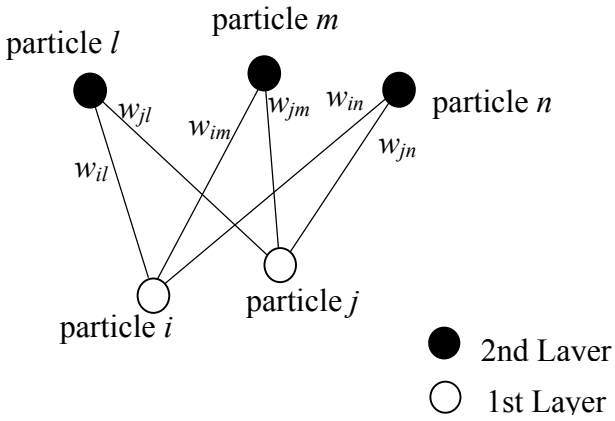

(b)

Fig. 6 Architectural illustration of the neural network model interconnecting all particles on the first image (i, j) and those on the second image (l, m, n).

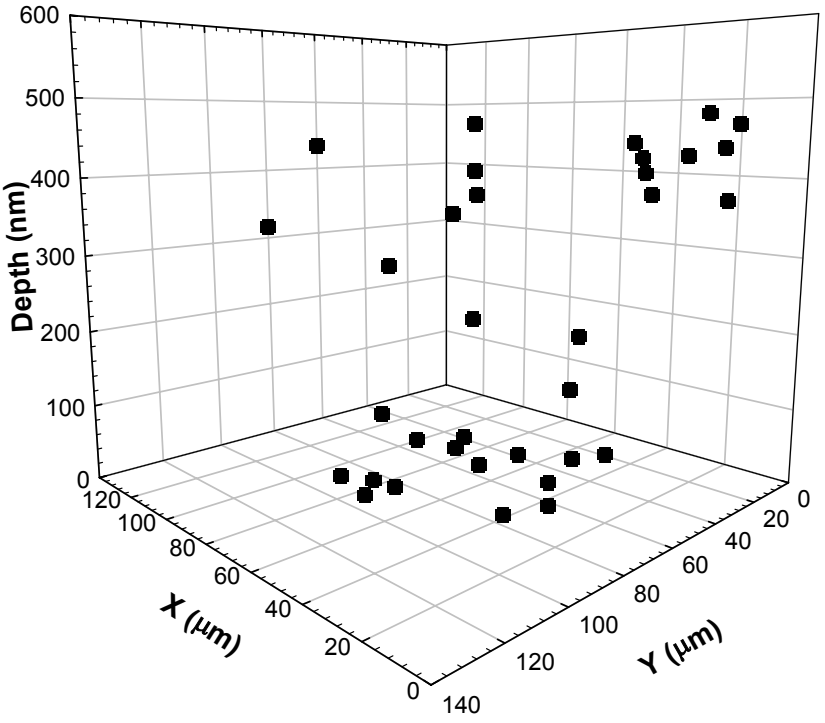

Fig. 7 Three-dimensional locations of 200-nm diameter fluorescent particles measured by R-TIRFM imaging analysis ($\theta_i = 62°$).

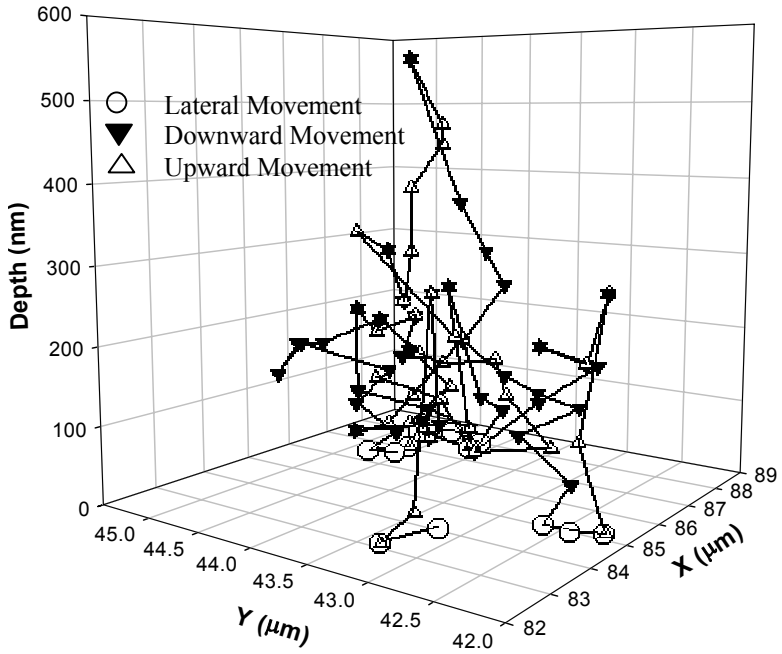

(a)

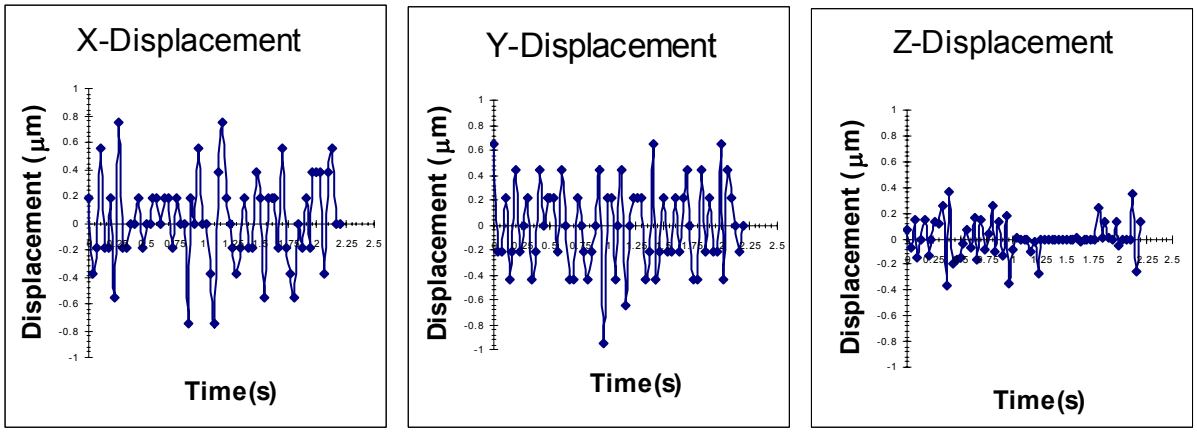

(b)

Fig. 8 Manual tracking of the Brownian motion of a single 200-nm particle suspended in water at 293K: (a) the history of three-dimensional locations over 67 imaging frames recorded for the duration of 2.23 s; and (b) the history of its *x*-*y*-*z* directional displacements.

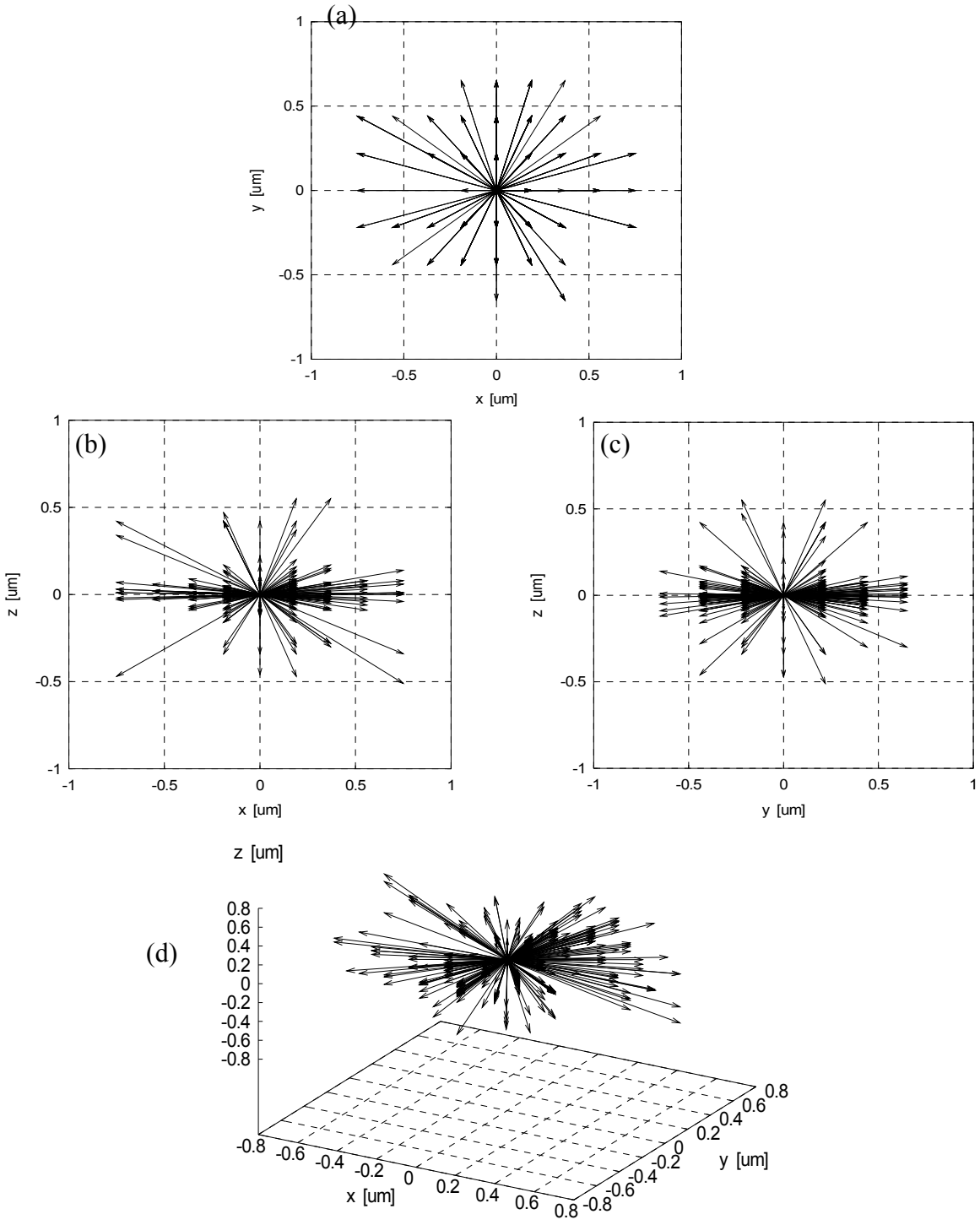

Fig. 9 Brownian diffusive displacements for multiple 200-nm particles tracked by the network model: the anisotropic displacements in the lateral *x*-*y* plane (a), the normally quenched displacements in the line-of-sight *x*-*z, y*-*z* planes (b and c), and the three-dimensional displacements (d).

Table1. Comparison of theoretical predictions with measured data for Brownian motion of 200-nm particles in water at 20°C for a specified time interval of 33-ms [free diffusion coefficient (D), hindered elementary (normal: $D_\perp$, lateral: $D_\parallel$), and hindered bulk diffusion coefficients (D_o)].

Parameters	**Units**	**Theory**	**Neural Network Based Multiple Particle Tracking Data**	**Single Particle Manual Tracking Data**
Mean Square Displacement (MSD)				
$< \Delta r^2 >$	μm^2	0.2753	0.2517	0.2278
$< \Delta x^2 >$		0.1022	0.1069	0.1024
$< \Delta y^2 >$		0.1022	0.1234	0.1008
$\mathbf{< \Delta z^2 >}$		0.0709	0.0214	0.0246
Brownian Diffusivity				
D	$\mu m^2/s$	2.1451	-	-
D_o		1.3765	1.2585	1.1390
$D_\parallel$		1.5330	1.7273	1.5240
$D_\perp$		1.0635	0.3210	0.3690
Mean Displacement				
$< \Delta r >$	μm	0	0.0208	0.0244
$< \Delta x >$		0	-0.0146	0.0167
$< \Delta y >$		0	0.0145	-0.0176
$\mathbf{< \Delta z >}$		0	0.0033	0.0030
Mean of Absolute Displacement				
$<\lvert\Delta r\rvert>$	μm	0.5247	0.4548	0.3791
$<\lvert\Delta x\rvert>$		0.3197	0.2987	0.2437
$<\lvert\Delta y\rvert>$		0.3197	0.3339	0.2761
$<\lvert\Delta z\rvert>$		0.2663	0.0786	0.0901